POLITECNICO DI TORINO

Master of Science in Civil Engineering

Master's Thesis

Investigation of the Carbonation Effect on the Microstructure and Transport Properties of Cement Pastes

Thesis Advisors:
Prof. Paola Antonaci
Eng. Giovanni Anglani
Prof. Erik Schlangen (*TU Delft*)
Dr. Branko Šavija (*TU Delft*)
MSc Claudia Romero Rodriguez (*TU Delft*)
MSc ir. Emanuele Rossi (*TU Delft*)

Candidate
Rui Ye

Hosting Institution
TU Delft – Microlab - Faculty of Civil Engineering and Geosciences

July 2019

Abstract

Carbonation is known to be one of the degradation mechanisms responsible for the corrosion of reinforcing steel, however, it is also capable to altering the microstructure of the cement paste. This study aims to study the effect of the carbonation on the microstructure and transport properties of ordinary Portland cement and blended cement paste. Accelerated carbonation at 5% CO_2 was used to carbonate the samples. The evolution of the spatial distribution of porosity was monitored using X-ray computed microtomography and compared with other methods such as MIP and gravimetric method. Then, the analysis was completed by coupling with other methods: thermogravimetric analysis TGA was used to evaluate the change of hydrated phases composition; dynamic vapor sorption DVS is used to complete the evaluation of the transport properties; random walk simulation to measure tortuosity of the pore network; LB simulation to assess the intrinsic permeability. Overall results showed a reduction of porosity and permeability following carbonation and an increase of tortuosity in both ordinary and blended cement paste. Moreover, it was found that using the dual CT scan method allows to mitigate the deficiency in term of resolution, and also a good alternative to traditional pore segmentation technique.

Table of Contents

1. Introduction

1.1 Research background

As we know, concrete is the most common used material for construction all over the world [1]. However, unlike other building materials such as steel, the microstructure of concrete, which determines most of its properties such as strength and durability, does not remain constant over time. In fact, the microstructure of concrete still develops during its service life; however, deterioration due either to external or to internal factors can alter the microstructure properties as well, and consequently its durability. According to ACI Committee 201 [44], the durability of concrete is defined as its ability to withstand the deterioration process caused by its interaction with the environment.

Figure 1: Corrosion of the embedded steel [P.K. Mehta, P.J.M. Monteiro, 2006]

Generally, all the degradation mechanisms involve three main factors [51]: first of all, the presence of the water, which is capable of caring aggressive ions within the concrete. Moreover, the presence of water is needed for various internal concrete degradation process themselves; secondly, the rate of degradation largely depends on the transport properties of concrete, which in turn is strictly related to the pore structure of the hydrated cement paste such as porosity and connectivity of the pore network; lastly, the presence of aggressive ions: air, in fact contains carbon dioxide and oxygen, and the latter is required for the corrosion of the reinforcing steel. All these parameters are also capable of evolving with time, making the durability of concrete challenging to predict [4].

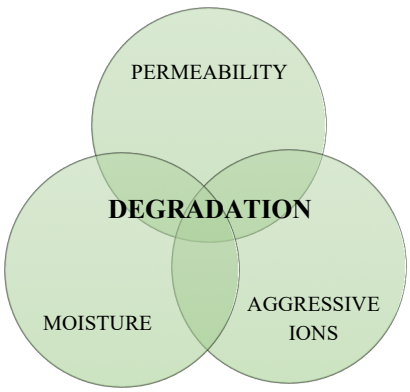

Figure 2: Main factors involved in the degradation mechanism of cement-based material [51].

Nowadays, durability characteristics of construction materials are continuously gaining more importance, also due to its high economic impact on society. The repair and maintenance costs of existing structures require about 40% of the total resources of the construction industry and keep growing every year [1]. Carbonation is one of the degradation mechanisms responsible for the corrosion of reinforcing steel, and

the latter is one of the major causes of concrete damage (Figure 1). It was reported by the U.S. Department of Transportation that 90 billion dollars were spent in 1991 for repairing damage caused by corrosion of reinforcing steel [1]. Regarding the concrete durability, carbonation of the hardened Portland cement paste reduces the pH of the pore water from approximately 13.5 to a value of about 9 (Neville 1997), leading to remove the thin oxide layer which covers and protect the steel bar from corrosion. In addition, to drop the pH of the pore solution, carbonation of Portland cement pastes alters its microstructure.

1.2 Objectives of the study

This study investigated the effects of the carbonation on the microstructure and transport properties of ordinary Portland cement and blended cement pastes, and its evolution in time, providing experimental data for further research as well as for modeling purpose. The investigation particularly focuses on porosity and pore size distribution, hydrated phases composition, water vapor sorption isotherms, permeability, and tortuosity.

Among microstructural characterization methods, nondestructive methods such as laboratory X-ray computed microtomography are acquiring popularity in the cement-based material investigation field. X-ray computed microtomography is a 3D imaging technique which allows to obtain a 3D reconstruction of the pore space without intensive sample preparation and more importantly, without altering the original pore structure of the sample. However, the use of CT for some problem investigation remains limited because of its inadequate resolution. Therefore, a new X-ray computed microtomography methodology (dual scan) will be validated with a view to extend the limited resolution of the tradition CT. Then, applied to the cement paste microstructure investigation as well as to the carbonation problem.

1.3 Research methodology

In order to validate the dual CT scan methodology, the porosity assessed before and after carbonation is compared to those of traditional methods such as Mercury Intrusion Porosimetry (MIP) and gravimetric methods. Then, the evolution of the microstructure of the cement paste and its transport properties at different CO_2 exposure times are monitored by means of the dual scan method coupled with other methods: thermogravimetric analysis TGA is used to evaluate the change of hydrated phases composition; dynamic vapor sorption DVS is used to complete the evaluation of the transport properties as well as of the pore structure of cement pastes, in terms of pore size distribution and water vapor desorption isotherms. Both experiments and simulations are used in this study.

2 Literature review

2.1 Microstructure of hydrated cement paste

Portland cement is a mixture of several compounds, but there are four principal constituents: tricalcium silicate $3CaO \cdot SiO_2$ (or C_3S), dicalcium silicate $2CaO \cdot SiO_2$ (or C_2S), tricalcium aluminate $3CaO \cdot Al_2O_3$ (or C_3A) and calcium ferro-aluminate $4CaO \cdot Al_2O_3 \cdot Fe_2O_3$ (C_4AF).

When anhydrous cement powder is mixed with water, a complicated series of chemical reactions take place leading to the formation of the microstructure, the so-called *cement hydration process*, which include:

- *Aluminates hydration*: the aluminates hydrate faster than silicates and causes the setting and the stiffening of the fresh Portland cement paste. Hydration of C_3A and C_4AF produce calcium-aluminates hydrates CAH.

$$C_3A + H_2O \rightarrow CAH \quad (1)$$

$$C_4AF + H_2O \rightarrow CA(F)H \quad (2)$$

- *Silicates hydration*: hydration of C_3S and C_2S produce calcium silicate hydrates CSH, calcium hydroxide (or portlandite) CH, and heat.

$$\begin{matrix} C_3S \\ C_2S \end{matrix} + H_2O \rightarrow CSH + CH\ (+heat) \quad (3)$$

The hydration of the Portland cement paste, as a result of the reactions (1), (2), (3) and (5), produce four principal solid phases, as shown in the Figure 3:

- *Calcium silicate hydrate (CSH)*: occupies up to 50 - 60 percent of the solid volume of the completely hydrated Portland cement paste. CSH does not have a well-defined composition as well as the exact structure is not known.
- *Calcium hydroxide (CH)*: also called portlandite, it occupies up to 20 – 25 percent of the solid volume. On the contrary, Portlandite has a definite stoichiometry, $Ca(OH)_2$, as well as the structure, in fact it forms large crystal with hexagonal-prism morphology.
- *Calcium aluminates hydrates (CAH)*: occupies 15 to 20 percent of the solid volume therefore it has a minor role in the hardened cement properties.
- *Unhydrated clinker grains*: it is possible to find it in the hydrated cement microstructure, and its presence depends on hydration degree and the particle size distribution.

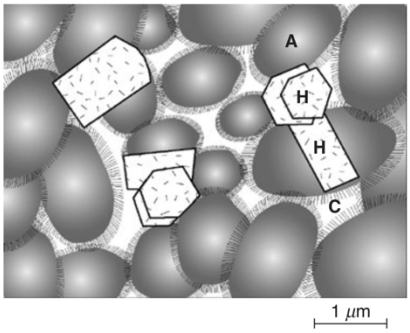

Figure 3: Hydrated Portland cement paste model: "A" represents CSH particles aggregation; "H" represents hexagonal crystalline products such as CH and CAH. "C" represents capillary pores or voids [P.K. Mehta, P.J.M. Monteiro, 2006].

As long as the solid hydration products are forming, a complex and tortuous pore network develops. As shown in Figure 4, in the hardened cement paste is possible to find an extensive pore size distribution, ranging from nanoscale pores to voids visible to the naked eye. Several classifications of the pore size were proposed, although a general subdivision into different classes of pores exists [3]:

- *CSH gel pore*: from approximately 0.5nm to 10nm in diameter and cannot be resolved by SEM.
- *Capillary pore*: from approximately 10nm to 10μm, can be resolved by SEM (Figure 5) and represents those voids that are not filled by the solid products of the hydration process.
- *Air void*: generally, are spherical in shape and represent the air that gets trapped in the cement paste during the mixing process.

Nevertheless, not all the pores are relevant to permeability, in fact, according to the classification of pores made by Mindess and Young (1981), only capillary pores with a diameter ranging from 0.5μm to 50nm are responsible for the water permeability, as shown in Figure 6 by Powers (1958), and furthermore those have to be connected. Finally, the topological properties of the pore network such as connectivity and tortuosity are more relevant for water permeability.

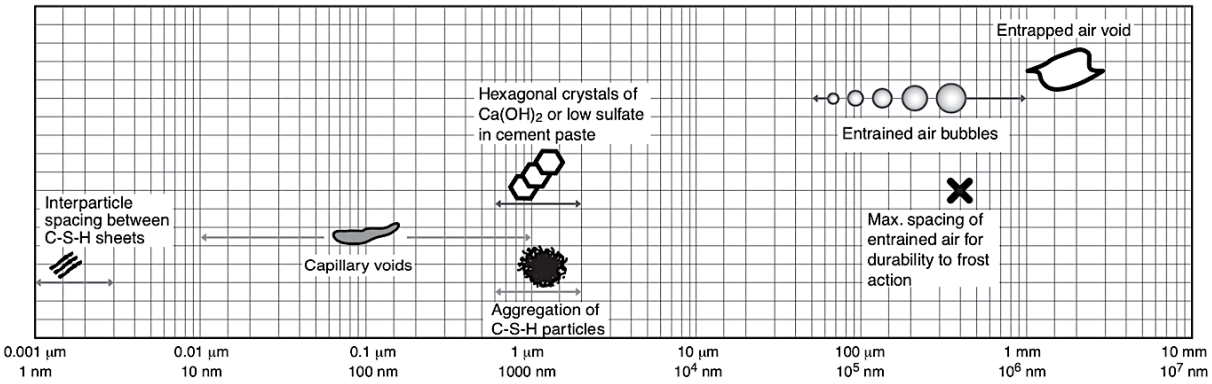

Figure 4: Range of pores in the hydrated cement paste [P.K. Mehta, P.J.M. Monteiro 2006].

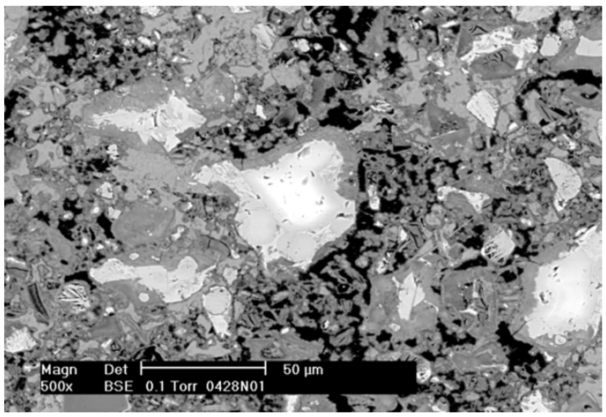

Figure 5: SEM BSE image of capillary pores (black) in the cement hardened cement paste [Guang Ye, 2003]

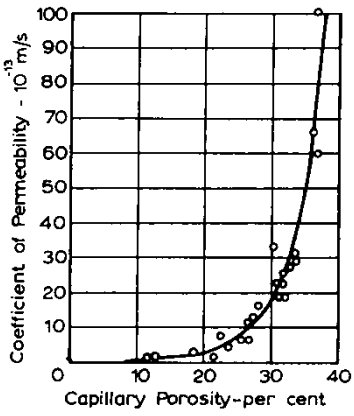

Figure 6: Relation between permeability and capillary porosity of cement paste [T.C. Powers, 1958]

It is well known that most of the chemical and physical process in cement involves the presence of moisture; moreover, the presence of a liquid phase is needed for the chemical reactions themselves,

including carbonation. During the drying processes, water is firstly removed from large pores such as capillary pores and then gradually proceed to empty pores with smaller size. Depending on the ease with which water can be removed, water exists in the following states:

- *Water in voids*.
- *Capillary water*: this water is divided, in turn, into free water, no change in volume occurs after its removal, and the water held by capillary tension, which causes shrinkage of the system once removed.
- *Adsorbed water*: this is the water which is physically adsorbed by the surface of solids and held by hydrogen bonding. It can be removed by drying to 30%RH and its removal cause shrinkage.
- *Interlayer water*: this water is present in the CSH structure held by hydrogen bonding and only a strong drying can remove it.
- *Chemically combined water*: it is part of the microstructure and it cannot be removed by drying.

According to the pore classification made by Jennings (2004) [43], during the drying process is possible distinguish four different pore size:

- Capillarity pore (75 nm): empty in the range from 100%RH to 90%RH.
- Large gel/mesopores (2-5 nm): empty in the range from 90%RH to 40%RH
- Small gel pores (1.2-2 nm): empty in the range from 40%RH to 20%RH
- CSH interlayer (<0.5 nm): empty in the range from 20%RH to 0%RH

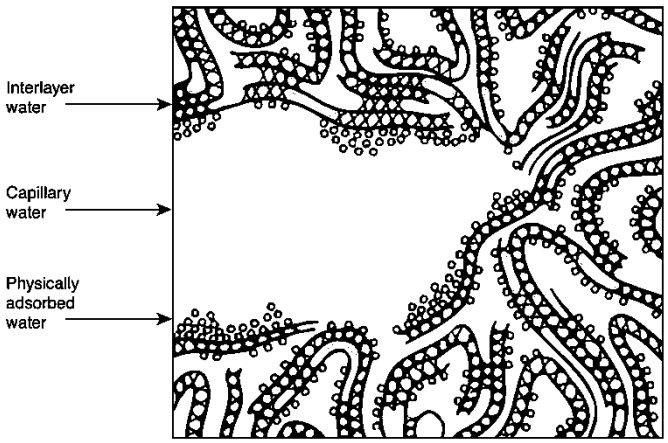

Figure 7: Model of the types of water associated with CSH [Feldman, R.F. and P.J. Sereda, 1970]

2.2 Microstructure of blended cement paste

Cost-saving and reduction of the environment impact of cement production led to the development of blended Portland cements; in fact, the production of cement causes more than 8% of the global anthropogenic CO_2 emissions [2]. The idea is to partially replace clinker by supplementary cementitious materials (SCMs), such as blast furnace slag (BFS), fly ash (FA), limestone powder and pozzolan. The production of blended cements nowadays, especially in Asia and Europe, has already exceeded the production of pure Portland cements [1].

The most important difference between Portland cement and blended cement is the *pozzolanic reaction*, which is the slow latent hydraulic reaction between pozzolanic material and calcium hydroxide (or portlandite).

Portland cement: $$C_3S + H_2O \xrightarrow{fast} CSH + CH \quad (4)$$

Blended cement: $$pozzolan + CH + H_2O \xrightarrow{slow} CSH \quad (5)$$

There are mainly three features of the pozzolanic reaction [1]:

1. The reaction is slow; therefore, the development of the strength will be slow, and consequently, the heat of hydration will be lower.
2. The reaction consumes portlandite, as shown in Figure 8, by replacing it with additional lower density CSH and therefore improve the durability in the acid environment.
3. The reaction causes a further refinement of the pore size (Figure 9) due to the formation of secondary CSH gel, therefore improves the strength and reduces the permeability.

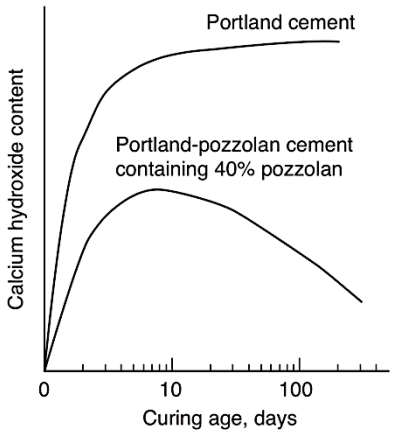

Figure 8: Comparison of curing age effect on the calcium hydroxide content between Portland cement and Portland-pozzolan cement [P.K. Mehta, P.J.M. Monteiro, 2006].

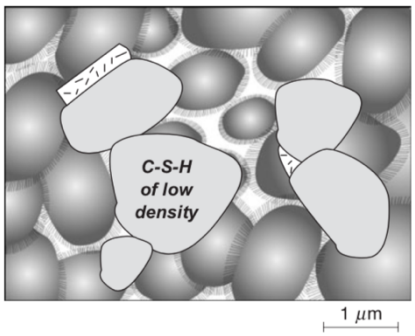

Figure 9: Hydrated Portland-pozzolan cement paste model. As a result of the pozzolanic reaction the pores size is refined [P.K. Mehta, P.J.M. Monteiro 2006].

2.3 Transport properties

As reported by Bouny V.B. [5], the global moisture-dependent transport coefficient is expressed as the sum of two transport modes. The first one is the advective transport of liquid water governed by the permeability, whereas the second one is governed by the diffusive transport of water vapor by means of the effective water vapor diffusion coefficient. Generally, at high saturation degree (S) range the liquid transport is prominent, vice versa at low S range the vapor diffusion is prominent; thus, it depends on the saturation state of the material. However, it was found that for weakly permeable material, such as cement-based material, water transport can be described using only the liquid permeability, neglecting the water transport in the gaseous phase [6].

The liquid water permeability is governed by the Darcy's law, which relates the liquid flow velocity with the pressure gradient of a fluid-saturated porous medium by means the permeability coefficient.

$$v = -\frac{K}{\mu} \cdot \frac{\partial p}{\partial x} \tag{6}$$

where v is the velocity, K is the permeability coefficient, μ is the dynamic viscosity of the fluid, p is the fluid pressure. Darcy's law is valid in the case of one single fluid phase, steady-state laminar flow, incompressible fluid, and no interaction between the fluid and the pore walls. In SI units permeability is expressed in area (m^2), but it is also expressed in Darcy unit, which corresponds to 0.987 x 10^{-12} m^2 or mDarcy (0.001 Darcy). However, the permeability coefficient in the equation 6 is express as a product of two terms $K = K_I \cdot k_{rl}(S)$, where K_I is the intrinsic permeability coefficient which is independent of the degree of saturation (can also be seen as the permeability of the fully saturated material), and $k_{rl}(S)$ is the relative permeability ($k_{rl}(S) \leq 1$), which dependent on the saturation state.

2.4 Carbonation

When CO_2 present in the air penetrates into the cement it dissolves in the pore solution, and it exists in chemical equilibrium with carbonic acid:

$$CO_2 + H_2O \rightarrow H_2CO_3 \tag{7}$$

The carbonic acid has two dissociation constants, first is for the dissociation into the bicarbonate ion HCO_3^-:

$$H_2CO_3 \rightarrow HCO_3^- + H^+ \tag{8}$$

The second one is for the dissociation of the bicarbonate ion into the carbonate ion CO_3^{2-}:

$$HCO_3^- \rightarrow CO_3^{2-} + H^+ \tag{9}$$

Therefore, because of the instability of the bicarbonate ion HCO_3^- in a high alkaline environment, it dissociates and forms carbonate ion CO_3^{2-}. The carbonate ions react with available Ca^{2+} ions in the pore solution, due to portlandite dissolution and lead to the precipitation of calcite:

$$Ca^{2+} + CO_3^{2-} \rightarrow CaCO_3 \tag{10}$$

Portlandite formed during hydration starts dissolving to compensate the decrease of the Ca^{2+} ions concentration due to $CaCO_3$ precipitation:

$$Ca(OH)_2 \rightarrow Ca^{2+} + 2OH^- \tag{11}$$

The dissolution of the portlandite is responsible for the pH drop of the pore solution. Furthermore, Ca^{2+} ion is also provided by the decalcification of the CSH gel described by the following reaction [7]:

$$(Ca)_x(SiO_2)(H_2O) + xCO_2 \rightarrow xCaCO_3 + SiO_2(H_2O)t + (z-t)H_2O \quad (12)$$

where the exact stoichiometric coefficients are not clearly defined, for instance it strongly depends on the initial Ca/Si ratio of the gel.

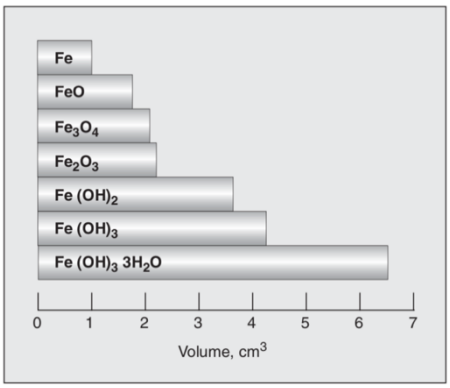

Figure 10: Transformation of metallic iron to rust is coupled by an increase in solid volume and the extent of expansion depends on the oxidation state [P.K. Mehta, P.J.M. Monteiro, 2006]

Regarding durability, carbonation is a degradation process of cement-based material since it decreases the pH of the pore solution activating the corrosion process of the embedded steel bar.
A high pH condition is required to keep the steel bar in a "healthy" state, also known as *passivation* state. In this condition, the steel bar is protected by a thin passivity layer of oxide, which prevent the steel from being in contact with oxygen and moisture. When the pH of the pore solution reaches values lower than 9.5, namely the depassivation threshold of the reinforcing steel, the thin oxide film starts to be removed, and corrosion can take place leading to the formation of higher volume oxides (Figure 10). The damage due to corrosion of the embedded steel bar can manifests in the form of expansion, cracking, and loss of cover as shown in Figure 1 [1].

Thus, commonly, carbonation is considered to be a deteriorating mechanism. However, apart from decrease the pH of the pore solution, which is considered as a passive/unwanted affect, carbonation of cement pastes can have positive (or active) effects [8]. Accelerated carbonation curing is one possible use; in fact, the exposure of fresh cement paste to elevated CO_2 concentration leads to achieve higher strength and improved durability compared to moisture curing. Furthermore, accelerated carbonation can be used to immobilization of certain types of waste in cementitious matrices. Finally, carbonation is the most efficient mechanism in term of autogenous healing performance of cementitious materials [9]: the precipitation of $CaCO_3$ as the result of the chemical reactions between Ca^{2+} (calcium ions) present in the pore solution and CO_3^{2-} (carbonate ions) dissolved in the crack water can bridge the two crack surfaces (Figure 11).

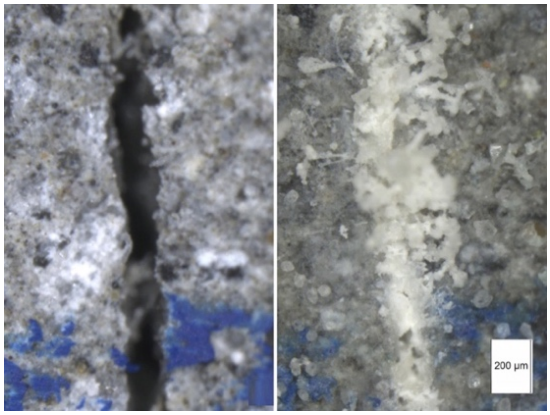

Figure 11: Autogenous healing mechanism: precipitation of calcium carbonate crystals in the crack [Gent University, Kim Van Tittelboom & Didier Snoeck], [45]

In terms of pore structure, carbonation refines the pore structure of Portland cement-based material due to the increase of the molar volume and precipitation of calcium carbonates in the pore network. In fact, in ordinary Portland cement $CaCO_3$ will precipitates in different polymorphs (aragonite, vaterite, and calcite), listed in Table 1. The extent of the porosity change depends on the polymorph formed, although the final form is the calcite, which is the more stable polymorph [8].

Mineral	Density (g/cm^3)	Molar volume (cm^3)	Variation of volume (%)
Portlandite	2.23	33.20	-
Calcite	2.71	36.93	11.2
Aragonite	2.93	34.16	2.9
Vaterite	2.54	39.40	18.7

Table 1: Variation of mineral's volume involved in the carbonation [http://webmineral.com]

Ngala and Page [11], observed a reduction in total porosity measured by Mercury Intrusion Porosimetry test after accelerated carbonation (5% by volume of CO_2, 65%RH and 20°C) of both ordinary Portland cement paste and blended cement paste (OPC/ 65%BFS).

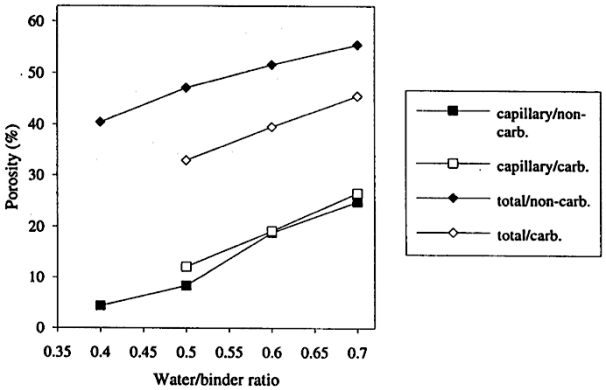

Figure 12: Porosity of non-carbonated and carbonated OPC pastes. [V.T. Ngala & C.L. Page, 1997].

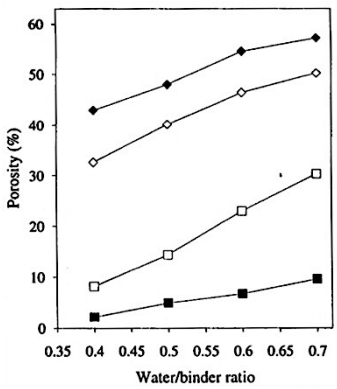

Figure 13: Porosity of non-carbonated and carbonated OPC/65%BFS [V.T. Ngala & C.L. Page, 1997].

No significant change in capillary porosity of ordinary Portland cement pastes after carbonation was found, whereas it increased in blended cement pastes, as shown in the Figure 13.

The influence of the carbonation on the transport properties is strictly related to the alteration of the pore structure. Nevertheless, the effect of carbonation on transport properties remains although poorly studied and data lacking, also due to the long experimental time required, and sometimes, the results are controversial [12]. Ngala and Page found an increase of chloride and oxygen diffusion coefficient following the carbonation of ordinary Portland cement [11], as reported in Figure 14. Other studies [12] observed a decrease in permeability of ordinary Portland cement pastes through the cup-method caused by pores clogging. It was also observed a drop of water content, in the water desorption curve, after carbonation, over all RH range. Phung et al. [13] found a drop of water permeability by a factor of six after 28 days of carbonation for ordinary Portland cement paste.

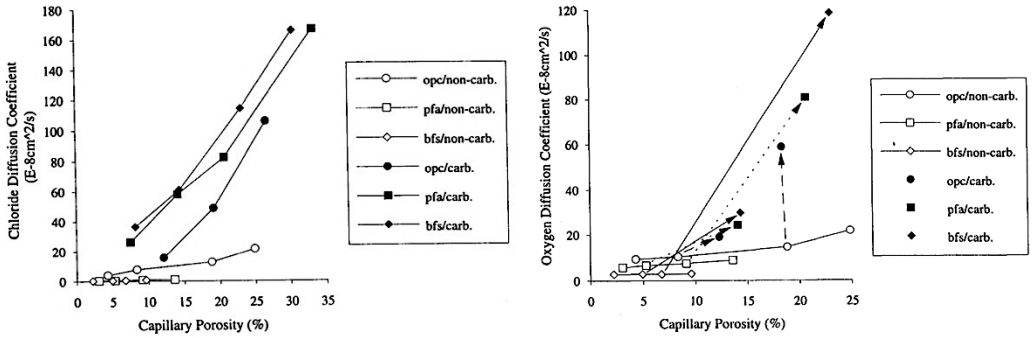

Figure 14: Chloride and Oxygen Diffusion coefficients of non-carbonated and carbonated cement pastes [V.T. Ngala & C.L. Page, 1997].

Transport properties of cement are fundamental in controlling the carbon dioxide diffusion rate, as well as the pore system of the hardened cement paste. The curing method is another influencing factor, and it was found that wet-cured sample performs better in term of carbonation depth than the dry-cured sample (Figure 15) [14].

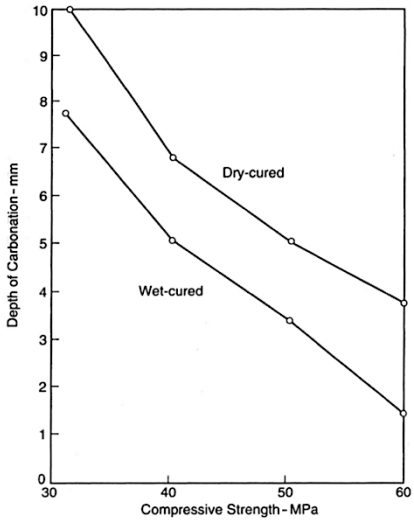

Figure 15: Effect of curing on depth of carbonation and compressive strength of concrete [Bassat, Nixon and Hardcastle, 1990].

Many studies focused on the environmental factors influencing the carbonation process, especially in terms of relative humidity (RH), temperature, and CO_2 concentration. Carbonation strongly depends on the moisture condition, and it was found that carbonation reaches the highest rate at a RH between 50% and 70% [13]. For the laboratory accelerated carbonation test, a limit of 20% of CO_2 concentration was set in order to be comparable with natural carbonation (0.04%) [15]. As a matter of fact, using higher concentration (more than 20%) involves different diffusion mechanism and it was found that compared with natural carbonation, carbonating at 10% leads to a progressive polymerization of CSH and forming Ca-modified silica gel and calcium carbonate, furthermore if the concentration is even higher (50%) CSH gel disappears completely [16]. Whereas using up to 3% of CO_2 concentration, the alteration of the CSH gel is comparable to natural carbonation conditions [41, 42].

2.5 Mechanisms of carbonation of slag blended cement

As a consequence of the pozzolanic reaction between slag and portlandite, a well-hydrated cement paste has a lower portlandite content. Therefore, the carbonation of CSH is the predominant mechanism in blended cement paste [10]. The secondary CSH produced by the pozzolanic reaction is defined as the low Ca CSH, and its carbonation produces a poorly-hydrated silica gel of a low molar volume leading to increase the porosity, although only a high replacement ratio of BFS (> 55%) caused an increase of the porosity.

This phenomenon was confirmed in many studies [10, 11, 29, 39].

Regarding the effect of carbonation on transport properties, Ngala and Page [11] found an increase of the diffusional properties after carbonation of slag cement paste, which was more effective respect to ordinary Portland cement as shown in Figure 14; in fact, the chloride diffusion coefficient increased by two orders of magnitude while the oxygen diffusion coefficient increased by one order of magnitude. A significant increase of permeability was obtained for the blended cement pastes despite the reduction in porosity in the study of M. Auroy et al. [12]. However, the formation of microcrack due to carbonation shrinkage significantly increased permeability.

3 Methodology

The following methodology was followed in this thesis:

1. Ordinary Portland cement and blended cement pastes were prepared with 0.6 water-binder ratio and cured for 90 days. Then, it followed 14 days of preconditioning period at 65% RH in order to reach the optimal internal condition for accelerated carbonation.
2. Prior to the accelerated the carbonation exposure dual CT scan, TGA and DVS were performed in order to assess porosity, hydrated phases composition, and water vapor sorption isotherms respectively. 3D microstructures of cement are obtained from microbeams scan, on which tortuosity and intrinsic permeability are simulated. Moreover, by means of the water vapor sorption isotherms, the unsaturated permeability coefficient and capillary pressure curve were obtained. All the properties assessed directly or indirectly in this stage represents the non-carbonated state.
3. Carbonation of the samples was done under accelerated condition.
4. All the tests listed in point 2 are repeated at different carbonation ages, namely 7, 14, 22 days. At each carbonation step, the sample was taken out from the carbonation chamber and analyzed as follows: dual scan to obtain the spatial distribution of porosity, TGA for chemical analysis and quantification of the portlandite and carbonates content, and DVS obtain the water vapor sorption isotherms. Moreover, both TGA and DVS are performed at different depth of the sample starting from the exposed surface, namely 3, 6, 9mm.

The validation of the dual scan method was carried out by comparing with the porosity coming from MIP test, which is widely used in characterization of the cement microstructure and thus its reliability is widely proven, although it is affected by some problems: first of all, since mercury is driven into the pores mechanically by applying a high pressure, MIP is considered as a destructive test; secondly, the data analysis is based on a cylindrical pore model, which is not necessarily true in cement-based material; finally, it cannot detect large pores and isolated pores [22].

Moreover, since direct methods to assess permeability are time-consuming, in a particular way for weakly permeable materials, in this study permeability are assessed coupling dynamic vapor sorption experiments (DVS) and computer-based simulations on the 3D microstructure obtained from microbeams. A comparison was carried out between an empirical model and simulated intrinsic permeability.

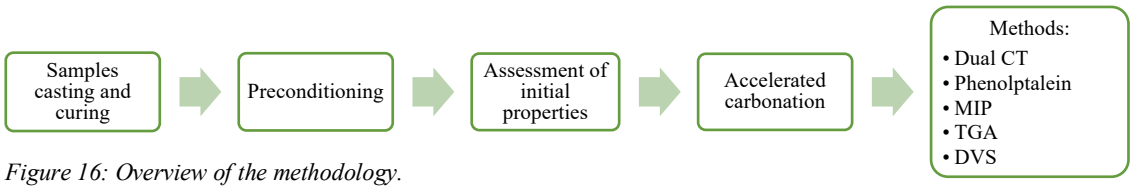

Figure 16: Overview of the methodology.

3.1 Materials and sample preconditioning

Two types of cement pastes were used in this work: ordinary Portland cement (CEM I 52.5R, EN 197-1), provided by ENCI B.V. (Netherlands), and ordinary Portland cement (CEM I 52.5R, EN 197-1) blended with 40%wt of Blast Furnace Slag (provided by ORCEM, Netherlands), with a water-binder ratio of 0.60. The amount of slag is such as to have comparable compressive strength with ordinary Portland cement paste at 90 days [17].

		Ordinary Portland cement			*Blended cement (40%wt slag)*		
Component	*Density [g/L]*	*Rel. volume [L/L]*	*Mass [g]*	*w/b*	*Rel. volume [L/L]*	*Mass [g]*	*w/b*
CEMI 52.5R	3500	0.32	1129.03		0.19	653.01	
BFS	2910	0.00	0,00	0.60	0.15	446.80	0.60
Water	1000	0.68	677.42		0.66	659.89	

Table 2: Mix design

All the pastes were prepared in batches of one liter and cast in polyethylene (PE) cylindrical vessels (approximately 5.80 cm diameter and 9.90 cm high). The same mixing procedure was used for all the pastes, which consisted of 4 minutes of total of mixing time in a planetary mixer. After pouring the paste into the vessels and sealed, all the cylindrical vessels were rotated (approximately 10rpm) for 24 hours in order to avoid bleeding and then demoulded [10].

Two curing methods were tested on ordinary Portland cement paste to investigate the influence of the curing method on the carbonation, namely moist curing and sealed curing. Moist curing method was done by placing the specimens in a high relative humidity room, in the so-called “fog room” (Figure 17), at almost 100% RH and 20°C. Whereas, sealed curing method consisted in keeping the material sealed into the polyethylene vessels until 90 days in ambient condition. Only moisture curing was used to cure the blended cement paste specimens instead.

All the specimens were cured for 90 days in order to obtain a high degree of hydration; thus, the change of the microstructure of the cement paste due to further hydration was excluded.

Sample name	Material	Curing method
OPC	Ordinary Portland cement	Sealed curing
OPS	Ordinary Portland cement	Moist curing
SLAG	Blended cement with 40% slag content	Moist curing

Table 3: Curing methods and sample name.

Figure 17: Moist curing of OPS and SLAG cylindrical specimens.

At the end of the curing period, approximately 1 cm x 1 cm x 4 cm prismatic shape samples (or "beams") were obtained from the core of each cylindrical specimen, as shown in Figure 18. Then, prior to the accelerated carbonation test, all the samples were conditioned at 65% RH and 20°C for two weeks in a desiccator. To reach the 65% of relative humidity, a saturated salt solution of $NaNO_2$ was used [18].

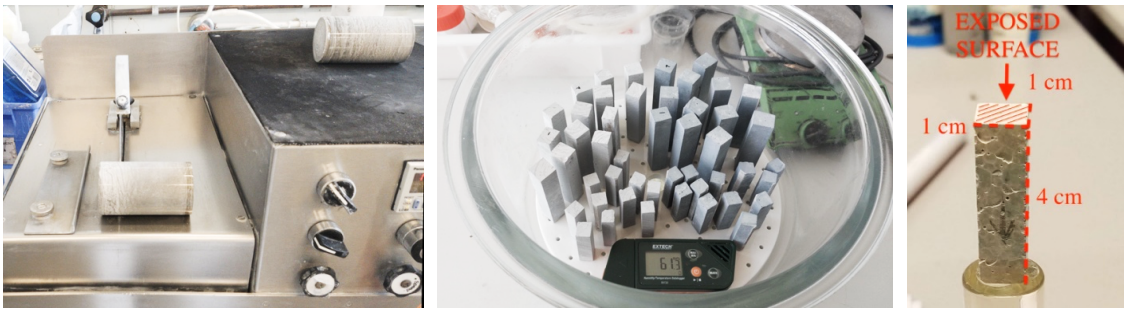

(a) (b) (c)

Figure 18: Sample preparation: (a) sample cutting, (b) conditioning, (c) sample size

3.2 Accelerated carbonation

Since natural carbonation is a very slow process, the carbonation process was accelerated by setting the optimal condition for fast carbonation. In this study, all the samples were exposed to an accelerated carbonation condition in the laboratory using 5% concentration of CO_2 (instead of 0.04% in natural condition) and 65% of RH. Under these conditions, the carbonation rate is maximal and comparable to a long-term carbonation in natural conditions [13]. It was estimated that an exposure period of 7-15 days to this condition is comparable to roughly one year of natural exposure [40].

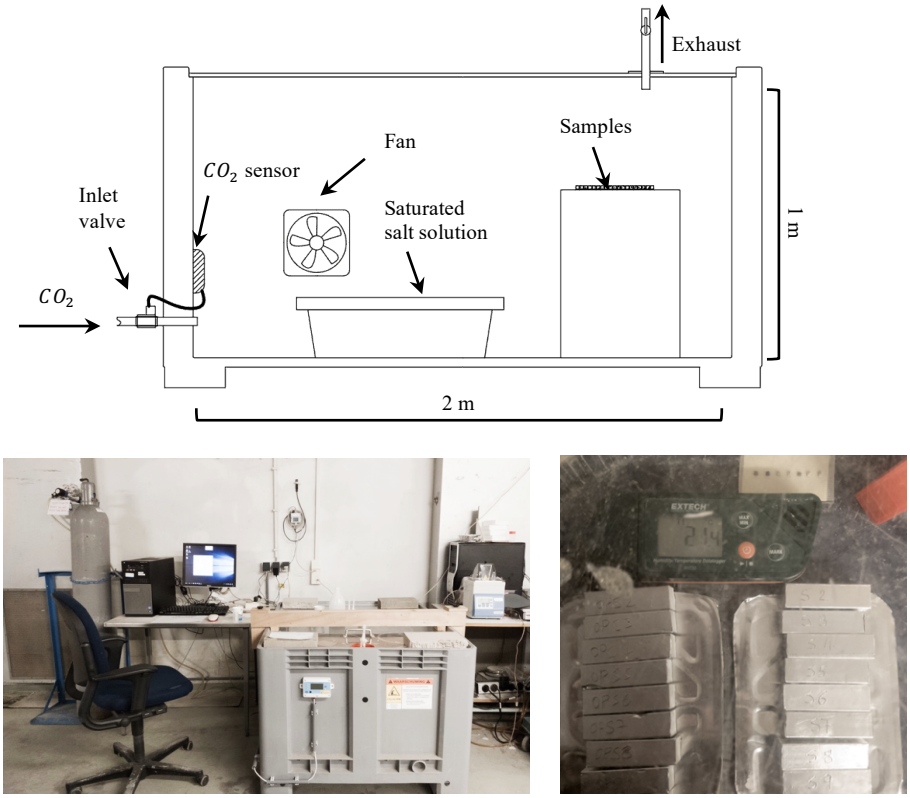

Figure 19: Carbonation chamber set-up

A controlled environment was created in the chamber (approximately 1 x 1 x 2 m), which is schematically represented in Figure 19. The RH is maintained constant in the box using a saturated salt solution ($NaNO_2$) and monitored by a sensor, whereas the CO_2 concentration is kept constant by means of a CO_2 sensor (provided by LogiCO2) that control the inlet gas flow into the box through a valve. Then, the box was placed in a 20°C temperature room. Both extremities of the "beam" are exposed to the CO_2 while the side is covered with an aluminum foil, in such a way the penetration of CO_2 is along with the sample height. Micro-beams were attached to a glass plate and placed in the chamber.

3.3 Mercury intrusion porosimetry (MIP)

Mercury intrusion porosimetry tests were carried out by using Micrometrics AutoPore IV 9500. The MIP test is used for measuring both porosity and pore size distribution of porous material. The sample is introduced into a chamber (Figure 20), and then mercury is progressively intruded into the porous structure under controlled pressures. The applied pressure is inversely proportional to the diameter of the pores according to the Washburn equation [1921] which correlates the applied pressure p (MPa) to the pore diameter d (µm) with the assumption that pores are cylindrical.

$$p = -\frac{4\gamma \cdot cos\theta}{d} \tag{13}$$

where p is the applied pressure (MPa), γ is the surface tension of the mercury (mN/m) and θ (-) is contact angle between mercury and the surface of the porous material (Figure 21).

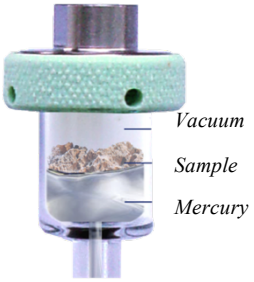

Figure 20: Penetrometer [https://www.micromeritics .com/]

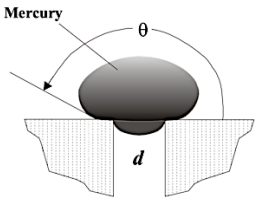

Figure 21: Contact model between mercury and pore [Guang Ye, 2003].

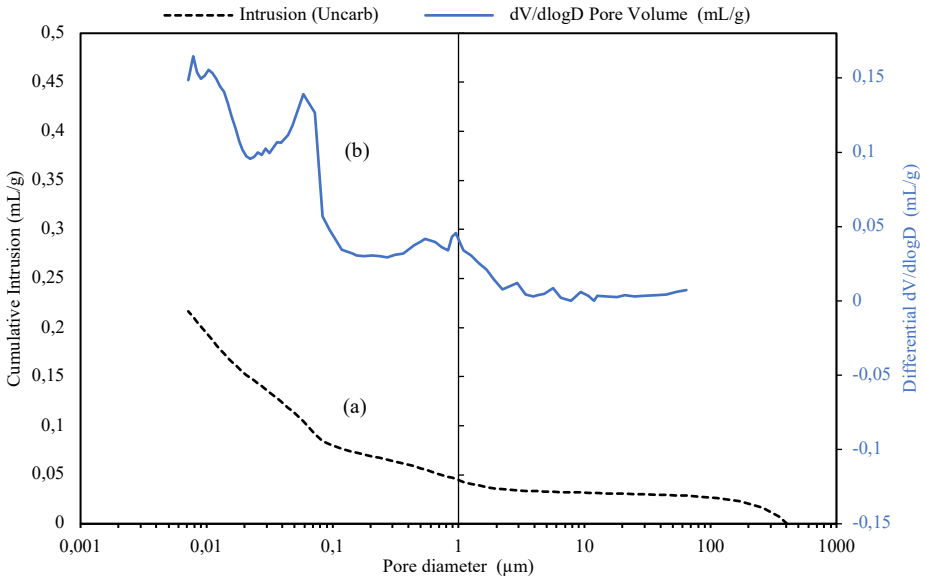

Figure 22: Typical pore size distribution: (a) cumulative curve, (b) differential curve

The volume of pores in a given size range is assessed by measuring the volume of mercury intruded into the sample for a given range of pressure. The machine can detect a change in volume of mercury of under 0.1µL. Therefore, the detectable pore range depends on the pressure range that the machine can apply. In this case, the maximal pressure of 210 MPa was applied, which corresponds to a minimal pore diameter of 7nm whereas the minimal pressure corresponds to the maximal pore diameter of 100µm.

By means of the MIP test, the total porosity is assessed from the total volume of mercury intruded divided by the bulk volume of the sample. Furthermore, the pore size distribution $dV(d)$ is determined by the equation:

$$dV(d) = -\frac{V_{por}}{d} \cdot \frac{dV}{dp} \tag{14}$$

The peaks found in the pore size distribution differential curve corresponds to the higher rate of intrusion for a given pressure change, and typically for the cement paste, a first peak is located between 0.01μm to 10μm and a second peak between 0.001μm to 0.01μm, which corresponds respectively to capillary porosity and gel pore [3]. Other three relevant parameters characterizing the pore structure can be determined:

- *Threshold pore entry diameter* d_{th}: defined as the intersection between the two tangents of the cumulative curve [19]. It is interpreted as the minimum diameter at which a continuous path through the whole sample can be found.
- *Critical pore entry diameter* l_c (or characteristic length): it corresponds to the pore size where the steepest slope of the cumulative intrusion curve is located [19, 20], and it is determined by the highest point on the corresponding differential pore volume curve. It is interpreted as the pressure at which mercury is able to penetrate into the interior of the sample [20].

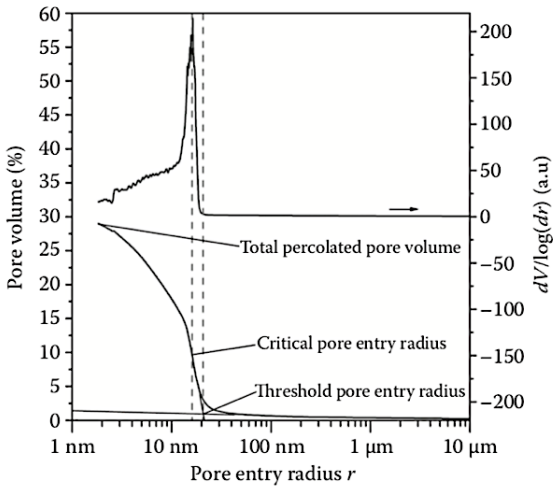

Figure 23: Assessment of total porosity, critical pore size and threshold pore size from MIP cumulative and differential curves [Scrivener, Snellings and Lothenbach, 2015]

- *Effective porosity*: it corresponds to the volume of mercury removed during the extrusion, as shown in Figure 24, and represents the effective path through which water can penetrate the cement paste.

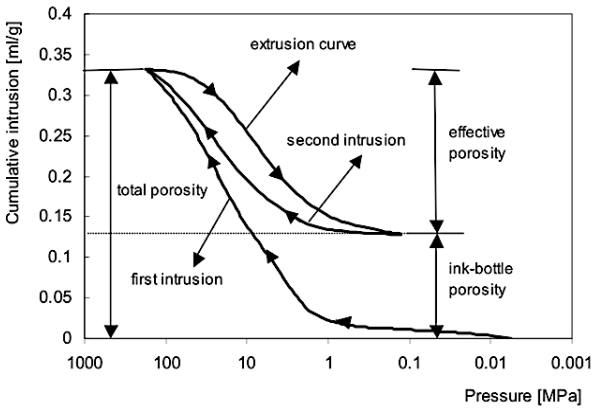

Figure 24: Assessment of effective porosity [Guang Ye, 2003]

Before the MIP test, the sample was cut in slices in slices of 3 mm of thickness and then dried by means of the solvent exchange method which is, according to many studies [21], the best way to arrest the hydration and dry the sample without altering the pore structure of the sample due to lower surface tension of the solvent. The soaking time depends on the sample thickness, and in this case, the sample was cut in slices of 3 mm and soaked for 7 days in isopropanol. After 7 days, the solvent was removed by diethyl ether for 24 hours and then followed by vacuum drying at ambient temperature for 1 hour. This procedure is also applied to prepare the sample for TGA test and DVS test [22].

Figure 25: Hydration stoppage by means of solvent exchange method

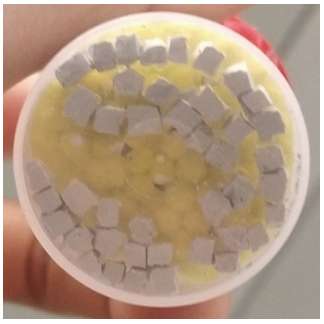

Figure 26: Storage of 3mm cubic sample

Once the sample is dried, for the MIP test, approximately 1 g of material is needed for each test. Therefore, the slices are broken into pieces of approximately 3 mm cube and then stored in a desiccator at 0% RH just before the test. Attention must be paid to prevent carbonation of the sample before the test thus, the operation must be done in a CO_2-free environment using a glove box (Figure 27).

Figure 27: CO^2-free box ("glove box") for sample preparation

3.4 Thermogrametric analysis (TGA)

Thermogravimetric analysis tests were carried out by using NETZSCH STA 449 F3 Jupiter. The test measures continuously the mass changes of the sample subjected to a constant increase of temperature (10°C/min) up to 1000°C, in a controlled argon atmosphere. A typical weight loss during TGA is shown in Figure 28. The test allows to determine the amount of different mineralogical components in hardened cement paste by knowing the typical temperature ranges at which decomposition of each component occurs [22]. The mass change recorded during the TGA is referred to the initial dry mass of the sample, obtained by solvent exchange method.

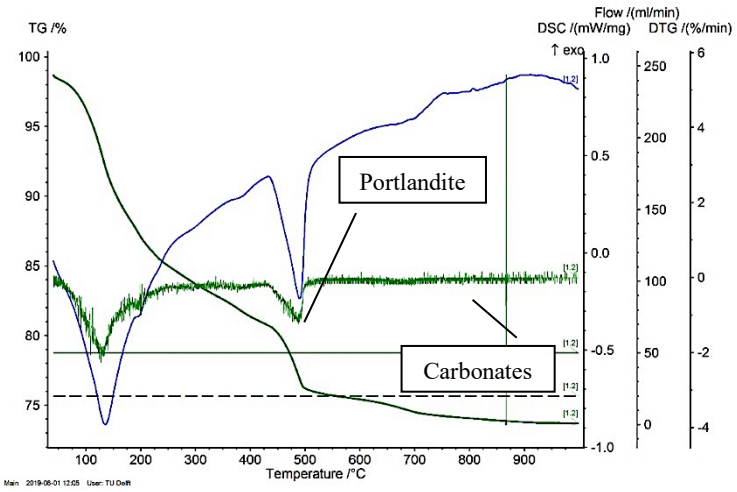

Figure 28: Plot of weight loss (%) recorded by TGA of ordinary Portland cement paste before carbonation test coupled with differential thermogravimetry DTG.

- *Portlandite ($Ca(OH)_2$)* decomposes between 400 and 500°C to CaO and H_2O, and by measuring the loss of mass due to evaporation of water, it is possible to calculate the amount of portlandite knowing the molar masses of portlandite ($M_{Ca(OH)_2} = 74\,\frac{g}{mol}$) and water ($M_{H_2O} = 18\,\frac{g}{mol}$):

$$Ca(OH)_2 = WL_{Ca(OH)_2} \cdot \frac{M_{Ca(OH)_2}}{M_{H_2O}} = WL_{Ca(OH)_2} \cdot \frac{74}{18} \tag{15}$$

- *Calcium carbonate ($CaCO_3$)* decomposes above 600°C to CaO and CO_2, and the amount can be calculated by measuring the mass loss and knowing the molar masses of $CaCO_3$ ($M_{CaCO_3} = 100\ g/mol$) and CO_2 ($M_{CO_2} = 44\ g/mol$):

$$CaCO_3 = WL_{CaCO_3} \cdot \frac{M_{CaCO_3}}{M_{CO_2}} = WL_{CaCO_3} \cdot \frac{100}{44} \tag{16}$$

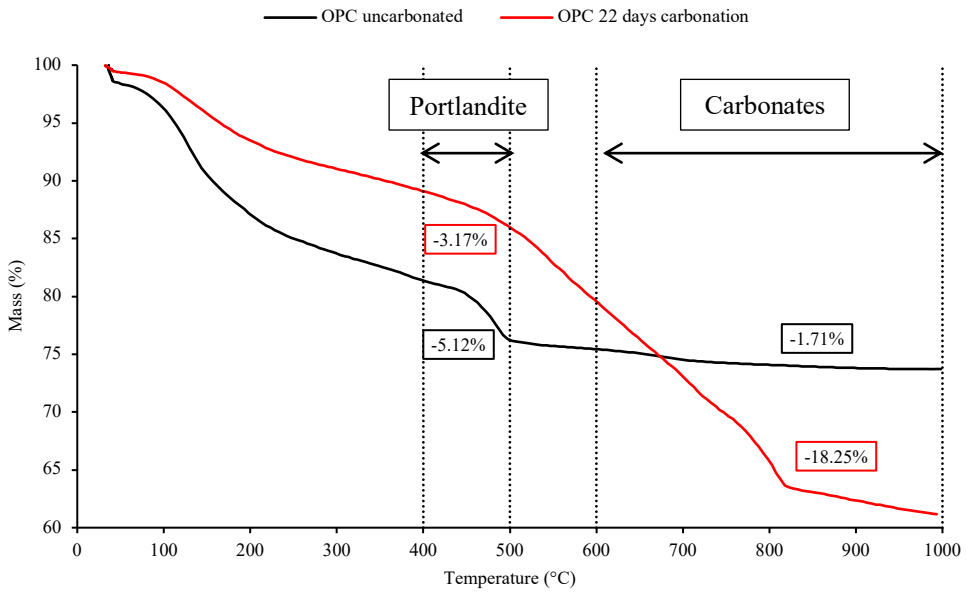

Figure 29: Weight loss referred to the initial (dry) mass of the sample of non-carbonated and carbonated OPC pastes during TGA test. Variation of mass in portlandite and carbonates decomposition range are marked.

In Figure 29, TGA results of non-carbonated and carbonated OPC pastes are reported as well as the weight loss in portlandite and carbonates decomposition range. Moreover, this technique is widely used to measure the hydration degree of the cement paste by measuring the chemically bound water content [23]:

$$W_c = (Ldh + Ldx) + 0.41(Ldc) \tag{17}$$

$$Degree\ of\ hydration = \frac{W_c}{0.24} \tag{18}$$

where Ldh is the weight loss due to dehydration (105 to 440°C), Ldx is the weight loss due to dehydroxylation (440 to 580°C) and Ldc is the weight loss due to decarbonation (580 to1100°C).

By means of the TGA, the profiles of the amount of portlandite (CH%) and calcium carbonate (Carb%) are obtained for 0, 7, 14, and 22 days of exposure period. Each value is the average value obtained by analyzing a 3mm slice cut staring from the exposed surface up to 9 mm of depth (as shown in Figure 30). Therefore, the carbonation depth assessed using this method is an overestimated value. The carbonation depth was assessed by measuring the depth at which the calcium carbonate content (carb%) is almost unchanged compared to its initial value (0 days). It must be noted that the calcium carbonate amount assessed by means of the TGA test might include those formed by carbonation of the CSH.

Prior to the analysis, the hydration of the cement paste has to be stopped by removing the water present in the pores. Solvent exchange following the same procedure explained in section 2.3 was used to stop the hydration. And then, fine powder is obtained from the slices by grinding the cement paste slices using a mortar (Figure 31). For each TGA test, approximately 50 mg of material was needed. The grinding operation, moreover, must be done in the glove box to avoid further carbonation of the sample.

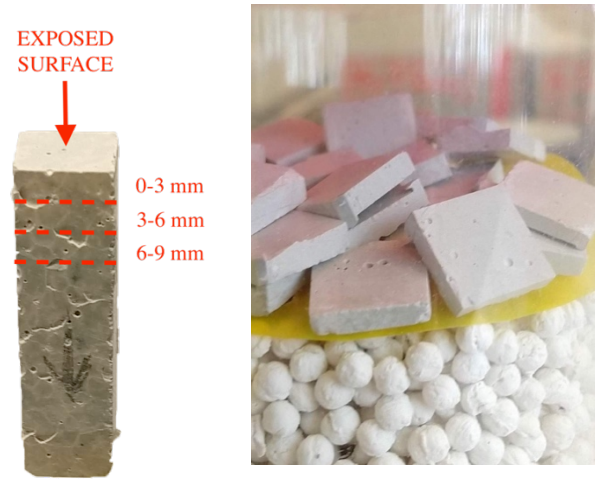

Figure 30: Sample preparation for experimental analysis

Figure 31: TGA powder preparation

3.5 Dynamic Vapor Sorption (DVS)

The Dynamic Vapor Sorption apparatus DVS Resolution, provided by Surface Measurement Systems, measures gravimetrically in time the mass water content for different relative humidities (RH) generated by mixing wet and dry N_2 gas, in order to avoid carbonation. The sample is placed in a sample pan, and the mass change due to increase or decrease of RH is monitored continuously in time by means of an ultra-sensitive microbalance which is capable to measuring changes in mass lower than 1 part in 10 million.

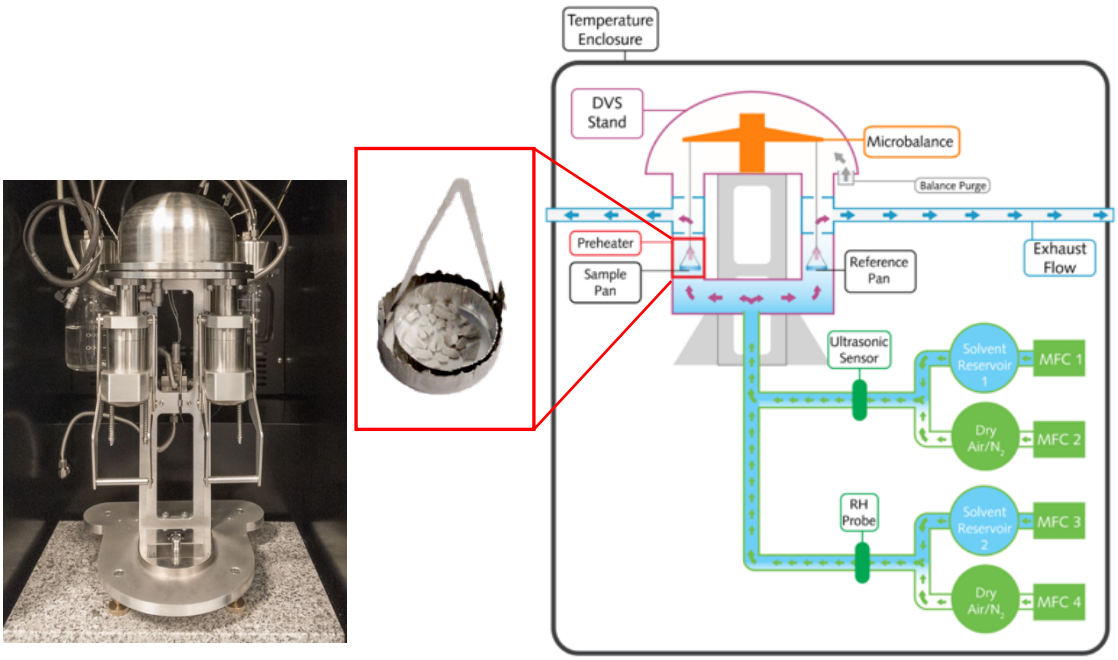

Figure 32: Schematic description of the DVS apparatus

A schematic illustration of the apparatus is shown in Figure 32. Thus, using an ultra-sensitive microbalance is time saving compared to the classical WVSI experiment (desiccator's method). An example of the mass change of the sample over time is shown in Figure 33: in this case, the plot represents a full cycle of adsorption and desorption. Each RH step ended when the equilibrium criterion was satisfied.

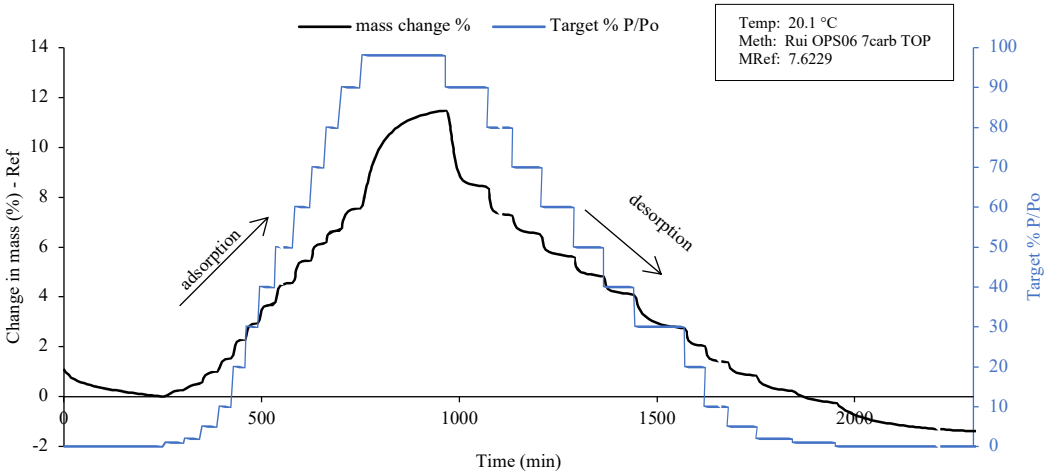

Figure 33: Typical plot of sample mass change due to adsorption and desorption of water. The dotted step function represents the relative humidity inside the DVS machine.

The DSV test allows to assess the water vapor sorption isotherms (WVSIs), which plot the equilibrium water mass content at a given RH and at a constant temperature (Figure 34). Each plot of WVSI represents an equilibrium state between the moisture content and the environment (RH and temperature), and the result shows a hysteresis between sorption and desorption caused by different pore filling between desorption and sorption. The water mass content is expressed as the water mass adsorbed by the sample at a given RH referred to the dry mass of the same sample assessed after the first step at 0% RH.

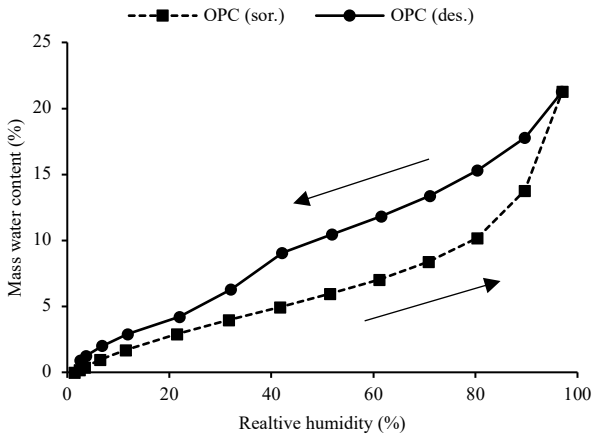

Figure 34: Water vapor adsorption and desorption isotherm measured at 20°C on ordinary Portland cement paste. The water mass content is expressed in percentage per unit mass of dry material.

For each sample approximately 10 mg of material (sieved using 500 - 1000 µm) was used for the test and a complete cycle of adsorption-desorption requires about 4 days, since the moisture uptake is a very slow process especially in the very fine pores, thus the time required to reach the moisture equilibrium in a sample depends on the sample size. Every cycle starts with 4 hours of conditioning at 0% RH and then the

RH is increased step by step until to reach 98% RH, namely 1 – 2 – 5 – 10 – 20 – 30 – 40 – 50 – 60 – 70 – 80 – 90 – 98% RH. The equilibrium state is satisfied when the sample mass change is lower than $0.002\,\frac{\%}{min}$ for 10 minutes, then the next RH step can start. The WVSI experiments can provide [4]:

- *CSH gel amount*: the CSH gel amount (cm^3 per g of dry material) is expressed as the ratio of the water adsorbed by the material at 22.8% RH (in g per g of dry material) to the water amount adsorbed by the CSH at 22.8% RH (in g per cm^3 of CSH). The latter was obtained by Olson and Jennings in [24] and listed in Table 4.

Material	water adsorbed by CSH (g per cm^3 of CSH)
OPC	0,207
25 wt% slag	0,238
50 wt% slag	0,213
75 wt% slag	0,212
100 wt% slag	0,170

Table 4: Amount of water adsorbed by CSH at 22.8%RH [Olson and Jennings, 2000]

- *CSH gel porosity*: based on the BJH method, it is possible to calculate the amount of CSH gel porosity in the material from the water content at 76% RH provided by the desorption curves, which associates the CSH gel pores with $d \leq 0.01\mu m$.

- *Capillary porosity*: it can be obtained assuming that capillary pores empty in the RH% range between 100% and 76%, therefore it is calculated as the bulk porosity minus the CSH gel porosity.

- *Bulk porosity accessible to water*: The bulk porosity accessible to water ϕ can be calculated as follow:

$$\phi = \frac{w_{des}(100\%\ RH) \cdot \rho_{app.dry}}{\rho_l} \tag{19}$$

where $w_{des}(100\%\ RH)$ is the water mass content at 100% RH obtained from the desorption curve, $\rho_{app.dry}$ is the apparent mass density of the dry material assessed by means of the hydrostatical weighing method, and ρ_l is the liquid water mass density (997 kg/m^3).

- *Water retention curve*: the water retention curve plots the water saturation degree S of the material against the external relative humidity (RH %). The liquid water saturation degree S can be deduced from the WVSI experiment, and it is expressed as follow:

$$S = \frac{w\,\rho_{app.dry}}{\phi\,\rho_l} \tag{20}$$

- *Capillary pressure*: The equilibrium state of the water in an unsaturated porous material is characterized by its capillary pressure; therefore, it is a property of any porous material. This capacity is related to the porosity of the material, and it can be seen as "the work required to transfer unit volume of liquid from the material at fixed water content to an external reservoir"

[20]. The capillary pressure p_c of the material can be derived from the desorption experiment by using the Kelvin equation, which expresses the liquid-vapor equilibrium in atmospheric condition ($p = p_{atm}$):

$$p_c = -\frac{\rho_l R T}{M} \cdot \ln(RH) \tag{21}$$

where ρ_l is the water mass density (997 kg m^{-3}), R is the universal gas constant (8.3144 J mol^{-1} K^{-1}), T is the temperature (293 K) and M is the molar mass of the water (18 g mol^{-1}).

In this study, the relative permeability is calculated by using the Mualem's model [5, 35]:

$$k_{rl}(S) = \sqrt{S}\,(1 - (1 - S^b))^{1/b})^2 \tag{22}$$

where b is a fitting parameter that can be obtained through fitting the analytical formula, proposed by Van Genuchten, on the experimental capillary pressure curve obtained from WVSI:

$$p_c(S) = a \cdot (S^{-b} - 1)^{1-1/b} \tag{23}$$

where a and b are fitting parameters depending on the microstructure of the material.

3.6 X-ray computed microtomography (micro-CT)

The micro-CT is a 3D imaging technique which allows to reconstruct an X-ray absorption's map from a series of X-ray projections. Among different techniques to characterize the cement paste microstructure, the X-ray computed tomography seems to be a promising method since it does not require intensive sample preparation and moreover, it is a nondestructive technique. Therefore, it allows to monitor the evolution of the microstructure in time without altering it. Nowadays, this technique is largely used to characterize the porosity of the cement as well as the connectivity of the pore network [25, 26, 27, 28].

The sample is mounted on a stick made of quartz and then clamped on a rotating platform between the X-ray source and the detector. The distance of the sample from the source is called FOD, while the distance between the X-ray source and the detector is called FDD (Figure 35). The voxel size of the CT image is related to the magnification which is equal to the ratio FDD/FOD.

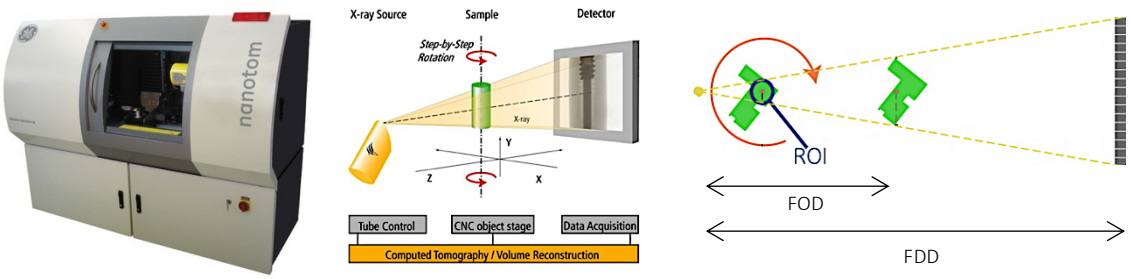

Figure 35: Schematic illustration of the CT scan equipment

The sample rotates 360° with an angle step of 1°, and for each position, 4 projections are acquired, in this case, with an exposure time equal to 0.5 seconds, therefore a total number of 1440 projections were taken. The working principle is based on the X-ray attenuation method. Each projection is a map of the resulting intensity of known unidirectional X-ray radiation after adsorption by the material. The reduction (or attenuation) in the intensity of the penetrating radiation can be represented by the Lambert-Beer's law:

$$I(y,z,\theta) = I_0 \cdot \exp[-\int \mu(x,y,z,\theta)\, dx] \tag{24}$$

where I_0 is the intensity of the X-ray beam before passing through the material; μ is the attenuation coefficient of the sample; θ is the angle of each projection. Therefore, the extent of intensity reduction depends on the composition and the path length, or in other words, it is related to the amount of material and the thickness of the sample. In this case, X-ray computed microtomography scans were performed with Phoenix Nanotom m (180kV/20 W X-ray NanoCT® system).

Scanning parameter	"big" beam	micro beam
Geometry		
FDD (mm)	300	500
FOD (mm)	42	6.3
Voxel size X (mm)	0.007	0.00063
Voxel size Y (mm)	0.007	0.00063
CT		
nr. Images	1440	1440
Rotation	360	360
Skip	1	1
Detector		
nr. Pixels X	2304	2304
nr. Pixels Y	2304	2304
Exposure time (ns)	500	500
X-ray		
Voltage (kV)	130	110
Current (μA)	210	90

Table 5: CT scanning parameters used

From all the 2D X-ray projections, the 3D volume is reconstructed by means of the built-in reconstruction software Phoenix Datos|x. Prior to the reconstruction, however, a beam hardening correction (BHC) must be applied to reduce beam hardening aarti-facts. Then, for volume rendering and images stack exporting the Volume Graphics VGStudio was used.

The reconstruction process converts the spatial distribution of X-ray linear attenuation coefficients into greyscale values (GSV). Each image is a spatial distribution of GSV, in case of 16-bit images GSV ranging from 0 to 65'535. The GSV is proportional to the X-ray attenuation coefficient: higher is the GSV, higher is the density of the material.

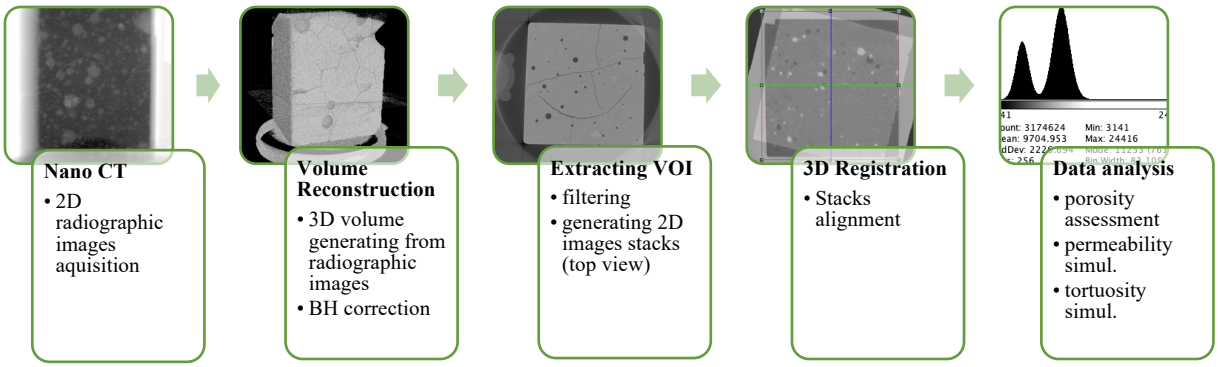

Figure 36: CT scan methodology.

Although micro-CT seems to be a promising method for the microstructure investigation, some problems limit its utilization. First of all, the maximum resolution of traditional CT scanners is not enough to resolve all the capillary pore size range and CSH gel pores, presently only synchrotron X-ray instruments are able to cover the submicron range. Moreover, it was shown that results are very sensitive to the image segmentation techniques, used to separate different components [27]. Currently, there is no standard procedure to perform such segmentation, although several segmentation routines have been proposed in the literature, and most of them are based on defining a range of GSV associated with the pore voxels [27].
As an alternative to the simple thresholding process to perform the pore segmentation, the "dual scan" method was used to separate pore voxels from the solid matrix. Furthermore, this technique allows to detect pores that goes below the resolution limit, by extending its resolution limit and applied to the study of the carbonation problem as well [29, 30].

The dual scan method consists of scanning the sample twice: the first in the original state (Figure 40a) and the second in the saturated state (Figure 40b). The saturation process was done in the vacuum chamber (Figure 37) and 0.05M of potassium iodide (*KI*) solution was used as a contrast medium [31], since water has a low attenuation coefficient similar to the air one. Then, the pore segmentation process was done by subtracting the two images of the same sample at different states, namely at saturated and original state.

Figure 37: Vacuum saturation equipment

The resulting 3D volume after the subtraction is a spatial distribution of porosity (Figure 40c): the voxel related to the solid material cannot be filled with the solution; therefore the resulting GSV after the subtraction is 0 (black), whereas if GSV is non-zero, it means that the voxel is filled partially or completely. The principle of the dual scan method is based on the additivity of the linear attenuation coefficient [32]. The GSV of each voxel in the original state is a weighted average of the values of air and solid material:

$$GSV_d = \phi^* \, GSV_a + (1 - \phi^*) \, GSV_m \tag{25}$$

where ϕ^* is the residual porosity of the voxel since the total porosity has to take into account also the presence of water in the pore (saturation degree), GSV_a and GSV_m are respectively the gray scale value of the air and the solid material. Once known the saturation degree (S) by means of the DVS test and the residual porosity ϕ^*, it is possible to calculate the total porosity:

$$\phi = \frac{1}{1 - S} \cdot \phi^* \tag{26}$$

In case of dried sample, the saturation degree is 0, thus the total porosity match with the residual porosity. In the saturated state the GSV of each voxel can be expressed as:

$$GSV_s = \phi^* \, GSV_{sol} + (1 - \phi^*) \, GSV_m \tag{27}$$

where GSV_{sol} is the gray scale value of the solution (KI). Rearranging equation 25 and 27 we obtain:

$$\phi^*(x, y, z) = \frac{GSV_s(x, y, z) - GSV_d(x, y, z)}{GSV_{sol} - GSV_a} \tag{28}$$

where ϕ^* is the residual porosity of each voxel in the position (x, y, z); GSV_s and GSV_d are respectively the gray scale value in the saturated state and in the dried state. Therefore, the calculation of the voxel's porosity by using the equation 28 requires a 3D registration process of the two scans, in such a way as to have the GSV before and after the saturation in the same spatial position (x, y, z). This means to calculate six degrees of freedom, as shown in Figure 39. The 3D registration is performed using DataViewer (Figure 38). The "target" stack (i.e. sample in the saturated state) is the one that has to be aligned to the "reference" stack (i.e. sample in the original state) by changing the six parameters (3 translation and 3 rotation) until the projections of the two samples on the three plane (xy, xz, yz) match perfectly.

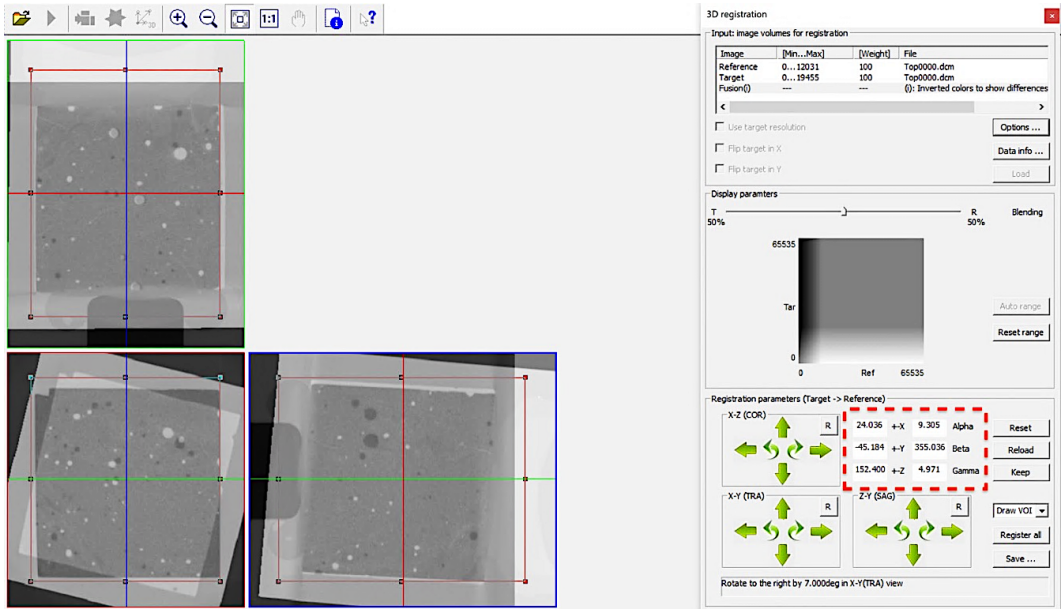

Figure 38: 3D registration process of the two different CT scans by using DataViewer.

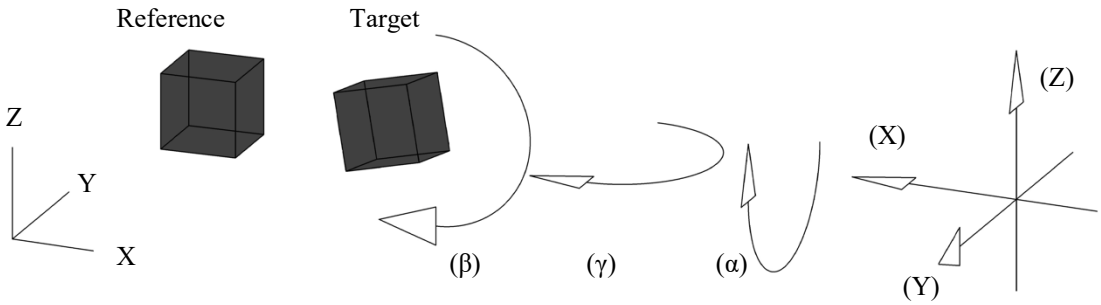

Figure 39: Schematica description of the 3D registration process.

Figure 40 shows the result after the registration. The sample in the saturated state (Figure 40b) is clearly brighter with respect to the original state (Figure 40a) due to its higher density after saturation. The subtraction of the two images, shown in Figure 40c, is done by using ImageJ as well as the data analysis,

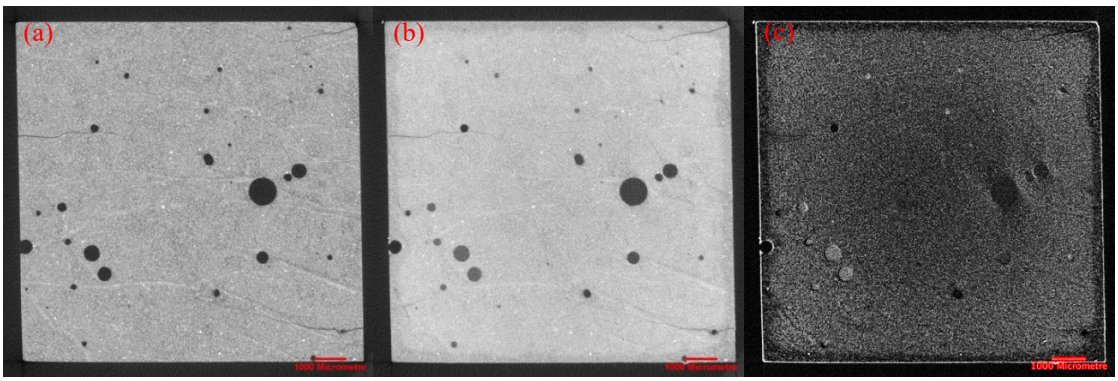

Figure 40: Typical registered CT images: (a) sample before the saturation, (b) sample after saturation, (c) subtraction between (a) and (b).

Both in the original state scan and in the saturated state scan, a vial containing the solution was scanned next to the sample (Figure 41). Firstly, to obtain the value of $(GSV_{sol} - GSV_a)$ which is used to normalize the GSV of the resultant images obtained after the subtraction process. Secondly, it was used as "reference" material to align the histograms of the original and saturated images stacks in order to compare the two independent scans.

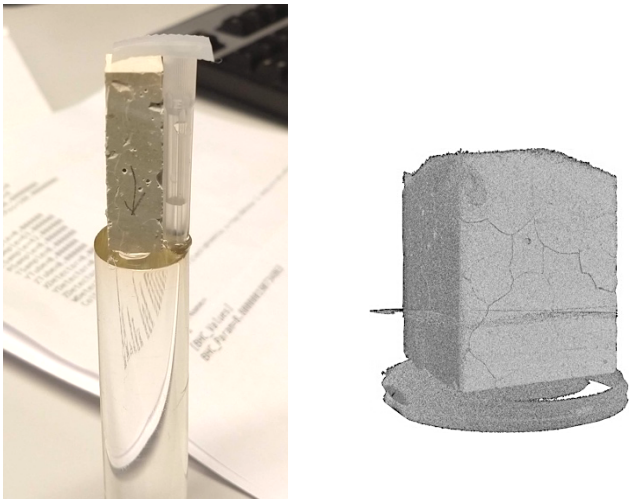

Figure 41: Mounting of the sample for the CT scan.
Reconstructed portion of the sample (right).

3D volume rendering of the porosity distribution can be to obtain by selecting multiple images as shown in Figure 42: for a better view, the porosity is represented in blue.

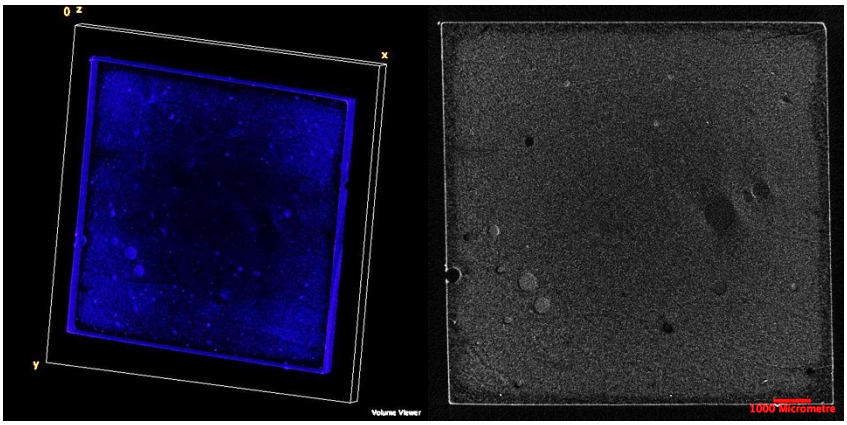

Figure 42: 3D volume rendering of the spatial distribution of the porosity.

The dual CT scans methodology, coupled with computer-based modeling, was used to perform micro-scale simulations of permeability and tortuosity and, for this purpose, tiny samples have been prepared [34]. From each material, a slice about 2 mm of thickness was obtained using a grinding machine, then by using a micro dicing saw, a series of "pillar" arranged in a grid is obtained (Figure 44). Each pillar has a square cross-section of approximately 0.5 x 0.5 mm whereas the height is about 1 mm (Figure 43).

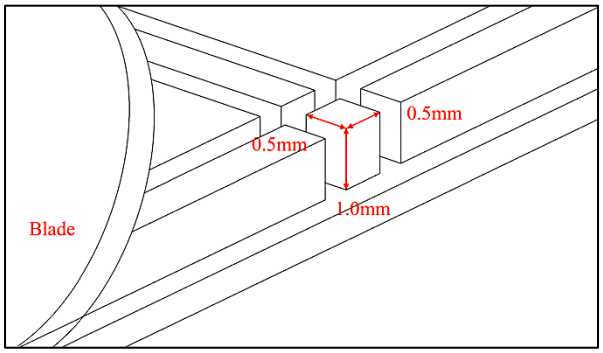

Figure 43: Schematic description of micro-beam sample preparation.

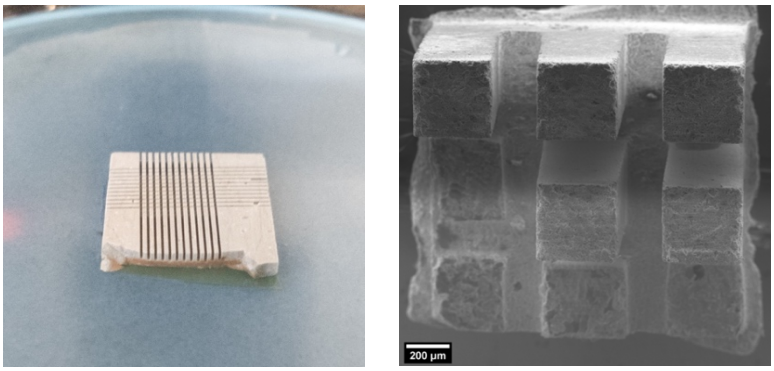

Figure 44: Fabrication of micro-beams and SEM image of pillars grid (right).

The pillar was then glued on the top of a quartz stick and scanned with a resolution of 0.63µm. Following the same procedure described in section 2.6.1, the dual CT scan was performed on the micro beam: the first scan at the original state then followed by the second scan in the saturated state. However, in this case, it was assumed that the first scan is done in the dried state because the scanning process causes an increase of temperature and consequently dry the sample, especially if the sample is very small. Therefore, the porosity assessed corresponds to the total porosity.

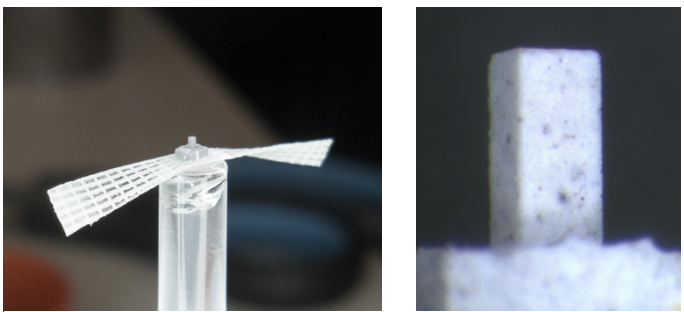

Figure 45: Sample mounting on quartz stick by using microscope. x40 magnification of the micro beam (right).

After the registration and the subtraction of the two scans, the pore segmentation is done by using the following criteria: each voxel that has a resulting GSV equal to 0 (black) is associated to solid matrix otherwise, if it is non-zero, is associated to pore space (white). In this way, it was possible to isolate the pore space from the solid matrix and convert greyscale images into binary images. Nevertheless, in this case, the porosity is overestimated since all the pores were assumed to be completely filled by the solution.

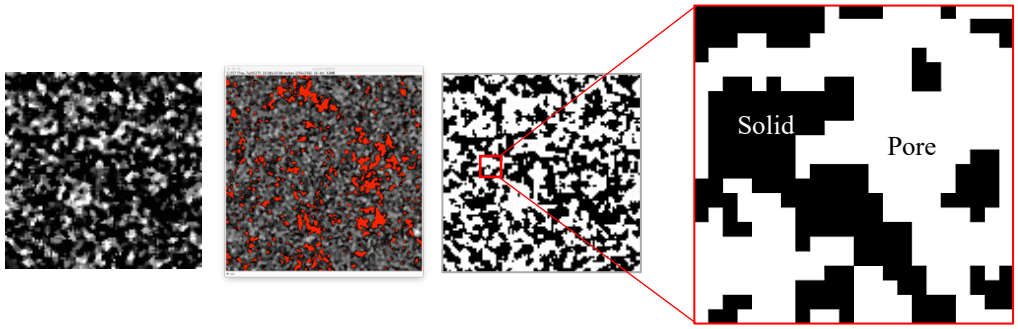

Figure 46: Segmentation process of the pore space: after subtraction of saturated and dried scan, the pore space is generated by thresholding all the voxels which has a non-zero GSV.

In order to reduce the computing time and the amount of memory, a volume of interest (VOI) of 256x256x256 voxels was extracted from each sample, as shown in Figure 48, which corresponds to a cubic volume of about 161.3^3 μm^3. Then both tortuosity and intrinsic permeability simulation were performed on the cubic sample.

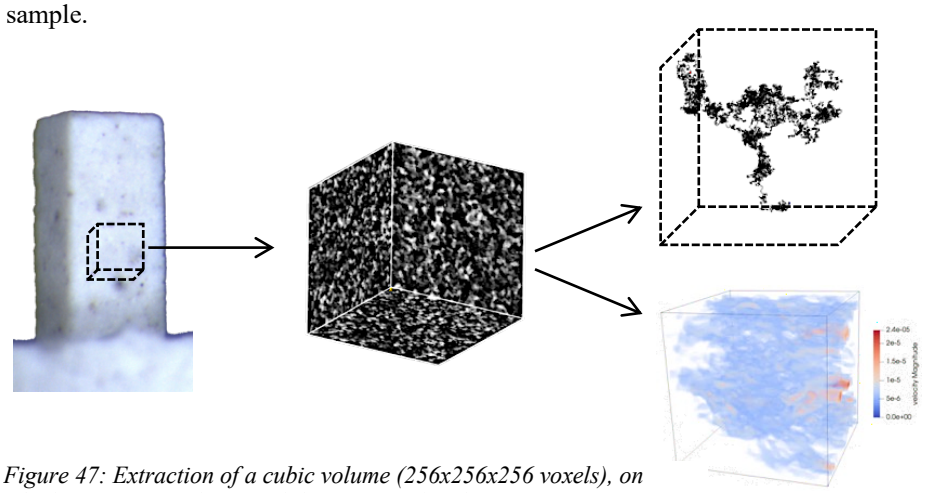

Figure 47: Extraction of a cubic volume (256x256x256 voxels), on which tortuosity and permeability are simulated.

3.6.1 Intrinsic permeability

The intrinsic permeability (or saturated permeability) is assessed by coupling X-ray computed microtomography and Lattice Boltzmann method simulations of Darcy's flow through a saturated porous medium carried out using Palabos [28, 47], an open-source Lattice Boltzmann solver. The dual CT scans method was used as an alternative to the ordinary segmentation process to separate pore voxels from the solid matrix. Then, the resulting 3D pore structure obtained from high-resolution X-ray computed microtomography imaging was used as input data for the simulations, providing the boundary conditions for the flow simulation.

Briefly, the Lattice Boltzmann discretized the Boltzmann equation, which describes the evolution of mass distribution of a single particle in a system: the physical space is discretized with lattice nodes (Figure 48)

and a finite set of microscopic velocity vectors are used to define the propagation of the fluid molecules (Figure 49), in this case, Darcy's law (equation 6) was used to describe the velocity data. The so-called distribution functions f are used to model the time and space depended on movements of particles, defining the density and velocity at each lattice node. The interaction with other particles, in terms of the change of the single particle's distribution function, is described by the collision integral function, which is the complex part of the Boltzmann equation. Thus, an important simplification was proposed by Bhathagar, Gross, and Krook (1954) and it approximates the collision operator with the so-called BGK approximation. Usually, for the 3D simulations D3Q19 (three-dimensional and nineteen-velocity), cube lattice structures are used [36].

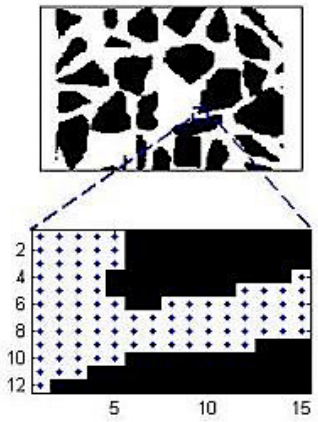

Figure 48: Lattice nodes at the center of each pore voxel [www.egr.msu.edu][46].

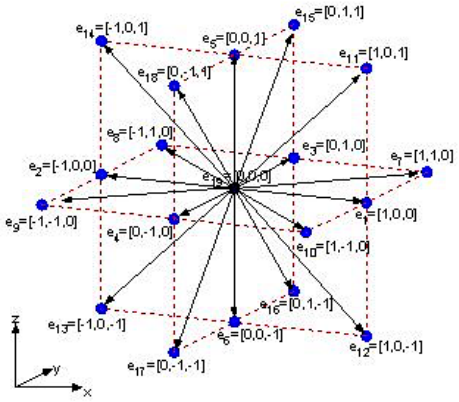

Figure 49: 3DQ19 lattice velocity directions model used in Palabos [www.egr.msu.edu][46].

The LB simulations consist of these main steps [37]:

1. Density and velocity are set to initial value in all lattice nodes.
2. Calculate the equilibrium distribution.
3. Collisions: collisions of different particles in the same lattice node and the original particle distributions moving in each direction will be redistributed according to the collision operator.
4. Streaming: the f_i in each node moves along the lattice velocity directions and arrives at its neighboring nodes.
5. Calculate new densities and velocities of the nodes.
6. If the difference of the average velocity of the whole domain between two consecutive time steps is lower than a threshold value, then the steady-state flow criteria are reached otherwise restart the cycle from step number 2.

In practical terms, the compute of the permeability using Palabos consists of three main steps [28]:

1. Convert the geometry defined by the binary images stack into bounce-back boundary conditions, which is imposed on the interface between solid and pore nodes (Figure 51): "0" (blue) for fluid voxel, "1" (light blue) for voxel that touches a pore voxel and "2" (yellow) for solid material voxel, as shown in the Figure 50.

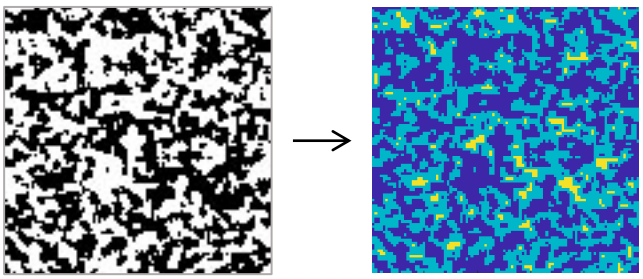

Figure 50: The binary input images are converted to bounce-back boundary conditions: "blue" for fluid voxel, "light blue" for solid-pore interface and "yellow" for solid voxel.

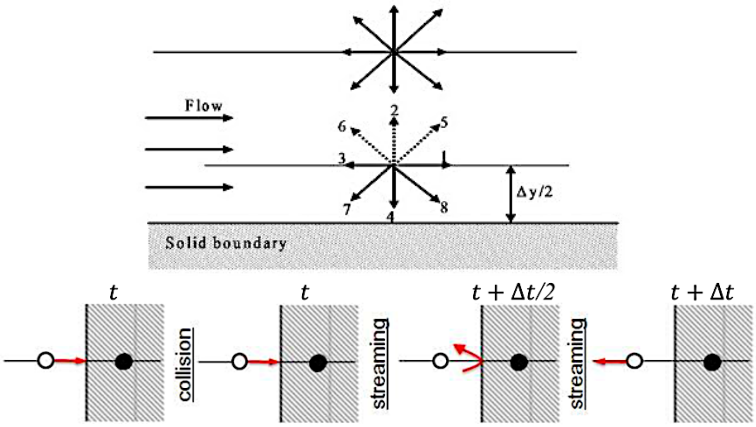

Figure 51: Schematic illustration of the bounce-back boundary condition: particle streaming from pore node to solid node scatter back to the por node along its coming directions [M. Zhang, 2013/ lbm.mcfernands.com]

2. Simulate, by imposing a constant pressure gradient between the inlet and the outlet, a stationary flow through the media. The steady-state is reached when the standard deviation of the average energy, measured at a fixed number of time steps, reaches a given threshold value. To ensure a laminar flow regime, each simulation has to run several times at different pressure gradients, and the permeability should remain constant. Figure 52 shows the resulting velocity distribution under steady-state condition obtained by imposing a pressure gradient 0.0005. Streamlines of the flow are shown in Figure 53.

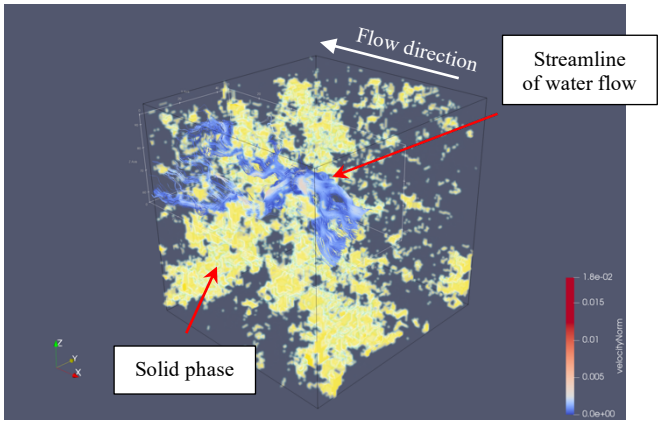

Figure 52: Velocity and streamlines of flow through the material.

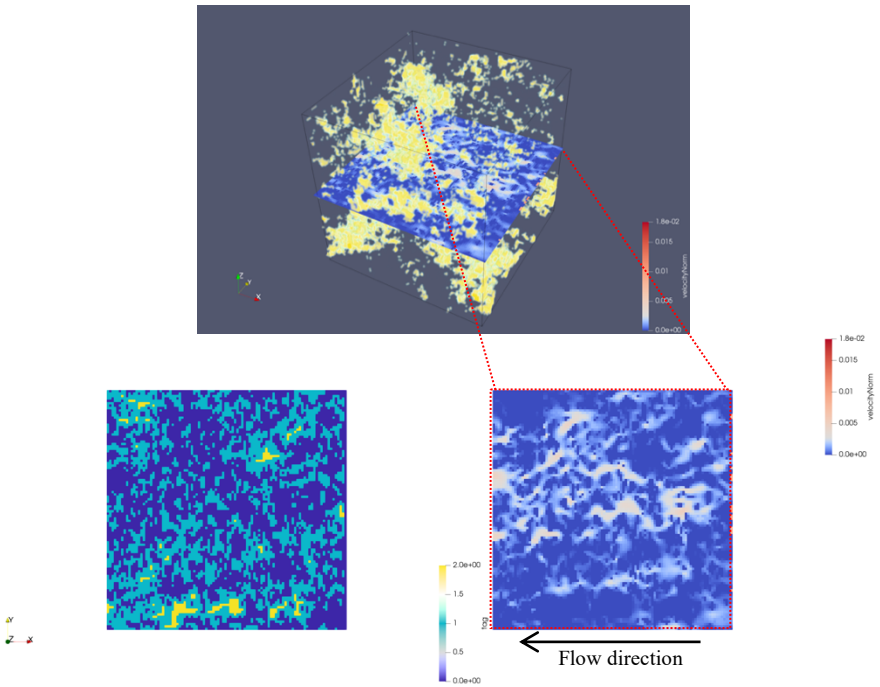

Figure 53: Slice of the geometric volume (left) and the resulting 2D velocity distribution under steady-state condition (right).

3. The computed permeability is expressed in non-dimensional lattice units; thus, to convert to real units it necessary to multiply with the square of the effective spatial resolution.

The intrinsic permeability coefficient can also be calculated by some physical models. The Katz-Thompson model (1986), is frequently used to predict the intrinsic permeability of cement-based material [3, 19]:

$$K_I = \frac{1}{226}\frac{\sigma}{\sigma_0} l_c^2 \tag{29}$$

where σ and σ_0 are respectively the electric conductivity of the saturated material and the conductivity of the solution in the pore, whereas l_c is the characteristic length of the pore system (or critical length). The ratio σ/σ_0 is also known as the inverse of formation factor F.

3.6.2 Tortuosity

The tortuosity of the pore network is an important parameter which influences transport properties [3, 20, 27, 38]. Geometric tortuosity τ_g, as shown in Figure 54, is defined as the ratio of the average length L_e of the geometric flow paths through the medium to the straight-line length L which is always shorter than L_e; thus, τ_g is always a number greater than 1.

$$\tau_g = \frac{L_e}{L} \tag{30}$$

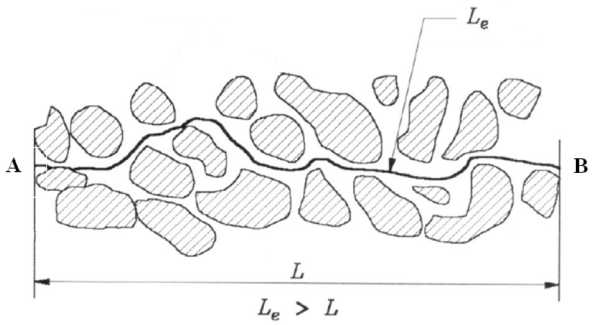

Figure 54: Geometrical tortuosity [Shackelford, C. D, 1991][50].

In this study, the geometric tortuosity is obtained performing a random walk simulation in the 3D pore space using high-resolution microtomographic images of cement paste [27, 33]. The program, developed by Y. Nakashima [available at http://staff.aist.go.jp/nakashima.yoshito/progeng.htm] [48, 49], simulates the diffusion of non-sorbing species (also called as walkers), such as water, by performing discrete lattice walks on the pore space and outputting the mean-square displacement of the non-sorbing walkers (r^2). The tortuosity is calculated as the ratio of the diffusion coefficient of the non-sorbing species in the free space (i.e. 100% porosity) to the long-time diffusion coefficient of these walkers in the pore space (Figure 56). By calculating the latter from the limiting slope of the mean square displacement r^2 averaged over n walker against time, the tortuosity results as [27]:

$$\tau_g = \left[\lim_{t\to\infty} \frac{dr^2(t)}{dt}\right]^{-1} \tag{31}$$

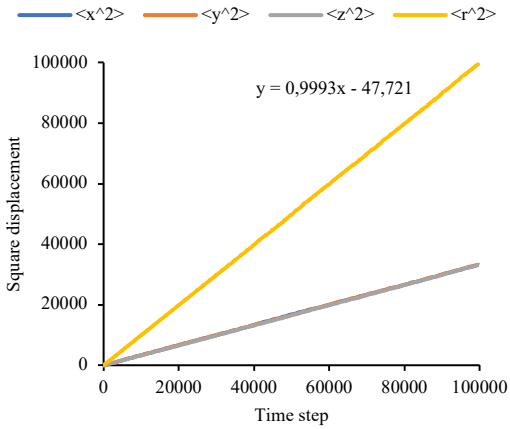

Figure 55: Plot of square displacement r^2 of averaging 50'000 walkers in free space.

The input data are the 3D CT images obtained from micro-beams following the same procedure described in section 3.6. In this case, the region of interest analyzed was 256 x 256 x 256 pixels where each voxel has a side dimension of 0.63 µm. The algorithm begins with choosing randomly pore voxel as a starting point at time step $t = 0$. Then, at time step $t + 1$ the walker executes a random jump to the nearest pore voxels, if the selected voxel as a solid voxel, the sump is not performed but the time still becomes $t + 1$ [27].

The main output of the program is the mean-square displacement $r^2(t)$ of the walkers as function of the time τ, as plotted in the Figure 55:

$$r^2(t) = \frac{1}{n}\sum_{i=1}^{n}[(x_i(t) - x_i(0))^2 + (y_i(t) - y(0))^2 + (z_i(t) - z(0))^2] \tag{32}$$

where n is the number of the walkers and $x_i(t), y_i(t), z_i(t)$ are the 3D coordinates of the walker's position at time t for the *i*-th walker. For all the random walk simulation, the number of the walkers was 50'000 and the maximum time step was 100'000, in order to allow walkers to travel a sufficiently long distance. By Nernst-Einstein relation, tortuosity τ, porosity ϕ and formation factor F, which describe the connectivity of the pore structure, are related to each other by the following relation [27]:

$$\frac{\phi}{\tau} = \frac{1}{F} = \frac{\sigma_0}{\sigma} \tag{33}$$

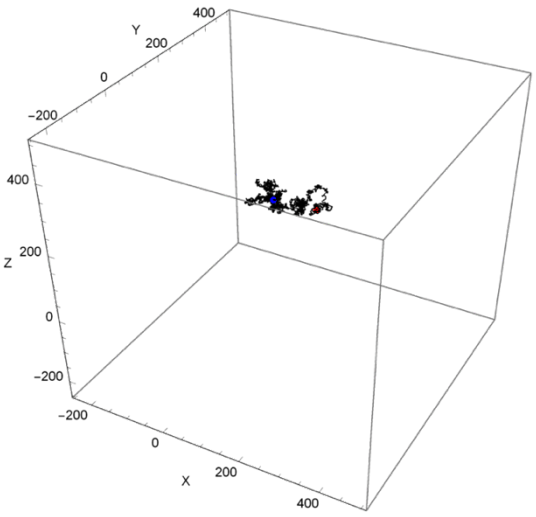

Figure 56: Example of 3D view of the trajectory of one walker in the pore space, its projection in the three orthogonal planes (at bottom).

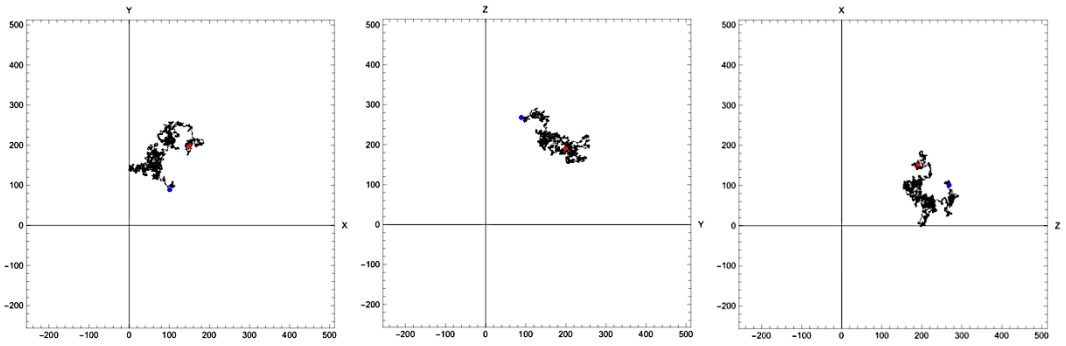

However, it must be noted that the tortuosity assessed by means of this method is just an indicative value and not precise because the resolution is not enough to resolve all the pore.

4 Results

4.1 Validation

The validation was carried out on OPC sample. Porosity was obtained before and after 22 days of carbonation by means of both MIP and dual scan method.

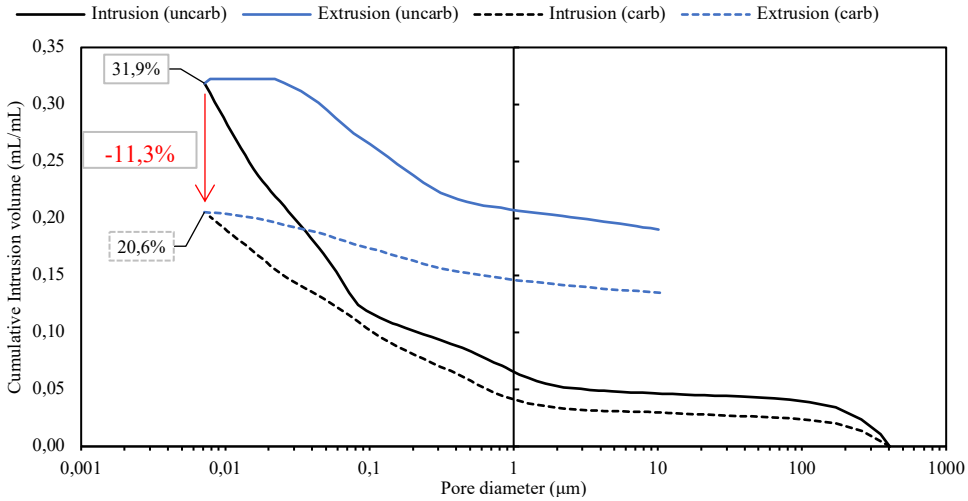

Figure 57: Pore size distribution of non-carbonated OPC (continuous curve) and carbonated OPC paste (dotted curve).

Based on the MIP results, the total porosity of the OPC uncarbonated and OPC carbonated samples obtained from the first intrusion curve (Figure 57) are respectively 31.9% and 20.6% which means a drop of the total porosity of 11.3% after 22 days of carbonation. The effective porosity calculated as the volume of mercury removed after the extrusion dropped by 5.8 % (from 12.9% to 7.1%). By analyzing the differential pore size distributions (Figure 58), it is very clear that the drop of porosity occurred mainly in the pore diameter range below 0.1µm.

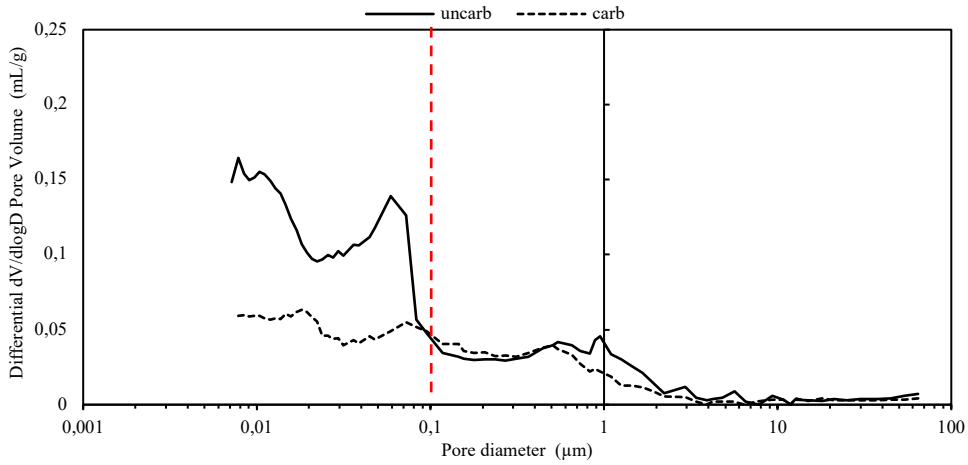

Figure 58: Pore size distribution differential curves of non-carbonated OPC (continuous curve) and carbonated OPC paste (dotted curve).

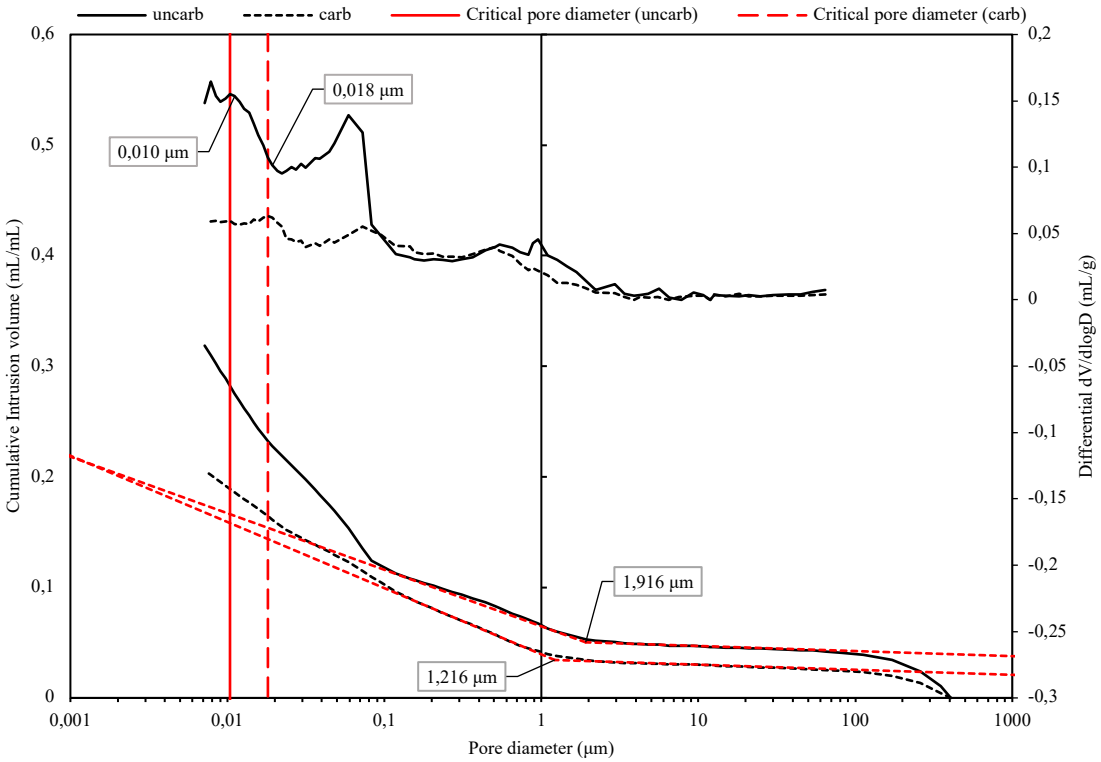

Figure 59: Change of critical diameter and threshold diameter following carbonation

The threshold pore diameter d_{th} calculated using the tangent method, decreased after carbonation from 1.916µm to 1.216µm, while the critical pore diameter increased from 0.010µm to 0.018µm (Figure 59). Table 6 summarizes the MIP results of non-carbonated and carbonated OPC sample.

OPC	Non-carbonated	carbonated
Bulk density [g/mL]	1,4718	1,7325
Characteristic length [µm]	0,010	0,018
Threshold diameter [µm]	1,916	1,216
Total volume intruded [mL/g]	0,2165	0,1186
Effective porosity %	12,90	7,10
Porosity %	31,86	20,55

Table 6: MIP results summary.

The first dual CT scan was performed in the non-carbonated state after 14 days of condition period in a desiccator at 65% RH. Then the second dual CT scan was performed on the fully carbonated sample, after 22 days of exposure in the carbonation chamber. Unlike other tests, no specific sample preparation was needed in the CT scans such as drying; thus, the measured porosity is the residual porosity. In order to obtain the total porosity, the saturation degree at 65% RH was obtained by means of DVS. Then, the total porosity before and after carbonation was obtained from the dual scan method as the weighted average porosity of a selected cubic volume, expressed as the sum of each porosity value multiplied by the number of voxels which has that value, and divided by the total number of voxels contained in the selected cubic volume.

Figure 60 shows the results after registration of the non-carbonated OPC sample. By analyzing the histogram of before and after saturation in Figure 60, (a) and (b) respectively, the change in GSV of the sample is clearly shown, in fact compared to the original sample the second peak of the saturated sample shifted towards higher GSV, whereas as expected the first peak referred to the air surrounding the sample, did not change in GSV.

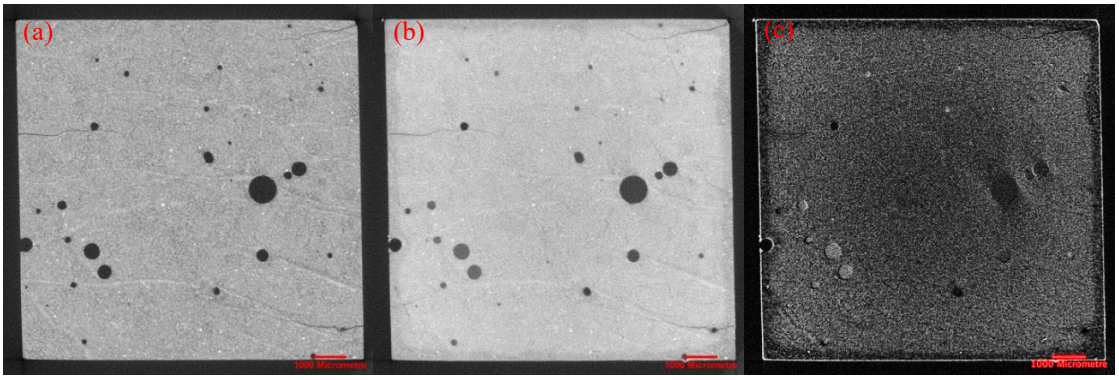

Figure 60: Typical registered CT images: (a) sample before the saturation, (b) sample after saturation, (c) subtraction between (a) and (b).

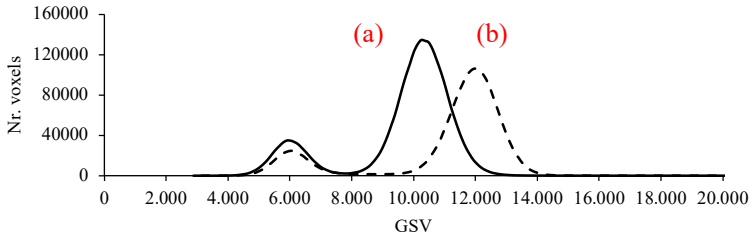

Figure 61: Histogram of (a) and (b).

In Figure 62, the results of the dual scan of non-carbonated (c) and carbonated sample (d) are shown, and its respective histogram in the Figure 63.

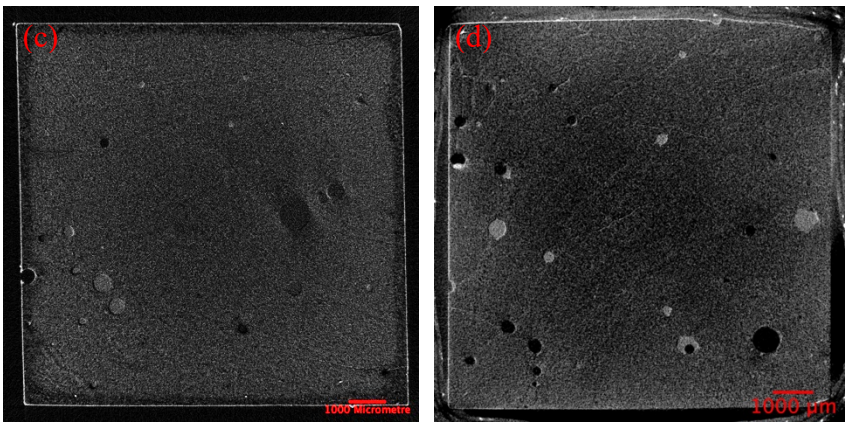

Figure 62: Results of the dual method of non-carbonated OPC (c) and carbonated OPC (d).

Both histograms presents a high peak of number of the voxels in correspondence of zero which means that those voxels are related to the solid material which did not adsorb solution, whereas the remaining voxels have a GSV in the range that goes from a value of 0 to approximately 2000 due to different moisture uptake capacity.

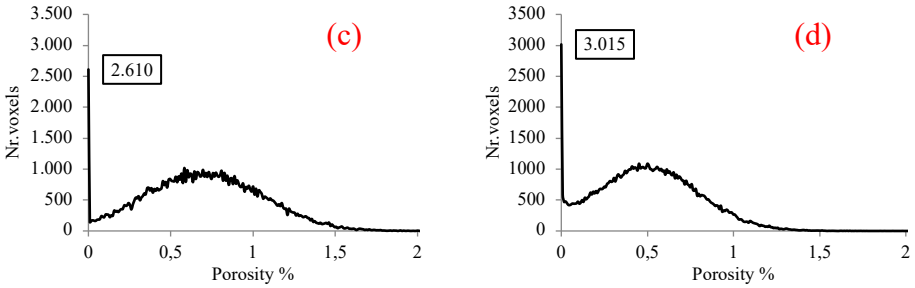

Average residual porosity = 30,42%
Average total porosity = 67,60%

Average residual porosity = 26,43%
Average total porosity = 60,07%

Figure 63: Porosity distribution of (c) and (d).

By analyzing the two histograms, it is possible to notice that after carbonation, the number of black voxels increased which means an increase of solid volume.

According to equation 28 it possible to obtain the distribution of the porosity of the voxels by normalizing the GSV. In order to proceed is necessary to measure the value of $(GSV_{sol} - GSV_a)$ which can be directly measured from some large pore filled with the solution (or scanning a vial filled with the solution): the value, in this case, is 1700. Therefore, all the values above 1700 mean that the porosity is more than 100%, which is nonsense. The 1st assumption was that all the voxels which have a value over 1700 were assumed to be equal to 1700. However, a second assumption can be made by assuming those voxels are related to noise, thus can be overlooked in the quantification of the porosity (2nd assumption).

Comparing with the results coming from traditional methods such as MIP and hydrostatical weighing, the dual CT's porosity is much higher. As shown in Figure 64, there is a good consistency of results between DVS and hydrostatical weighing assessed porosity, whereas in accordance with other authors the MIP porosity is always lower, because the range of pore accessible to mercury is narrower respect to water.

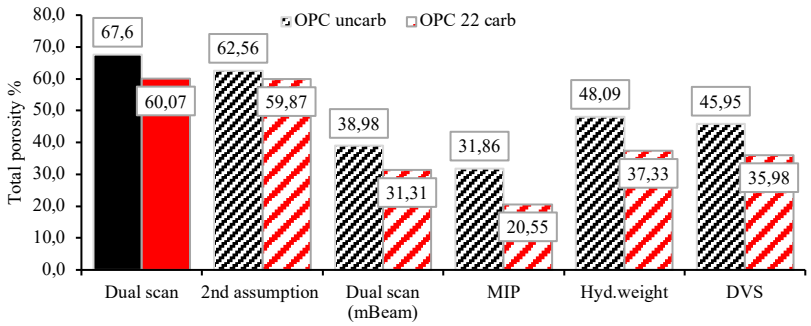

Figure 64: Total porosity measured before and after carbonation using different methods.

However, in line with the expectations, a decrease in porosity after carbonation of OPC was observed by all the methods. Moreover, based on the results of the MIP pore size distribution analysis, the dual CT scans method was able to detect the change in porosity which occurred mainly in the pore size range below 0.1µm, over one order of magnitude lower than the resolution of a single CT scan (7.0µm) as shown in the Figure 65.

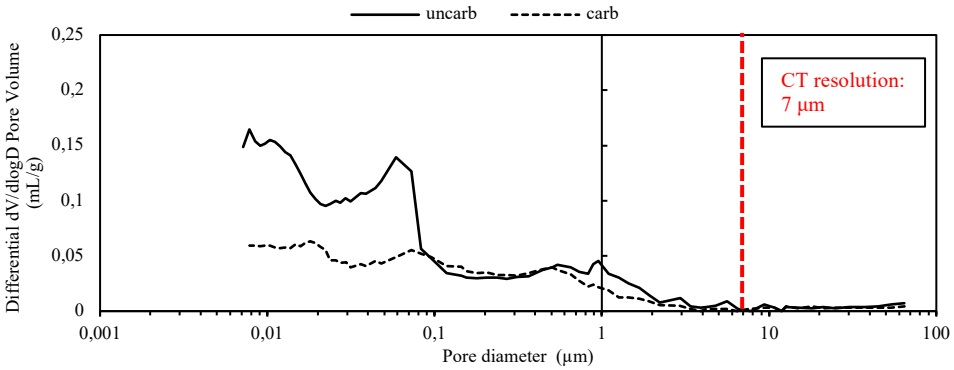

Figure 65: MIP differential pore size distribution before and after carbonation.

Some considerations about the dual scan's method can be pointed out, which could justify the final results:

- The saturation degree in the original state according to the DVS result is 55% (at 65% RH); thus, the attenuation coefficient of the original pore solution might be altered by the saturation process using the doping solution, and therefore leads to overestimating the porosity. This means that the potassium iodide solution, used to saturate the sample, mixed with the pore water and then in the second scan, the GSV of the original pore water was altered.
- Moreover, the presence of digital noise overestimates the porosity by 4.5%, even after applying a filter as evidenced in Figure 66.

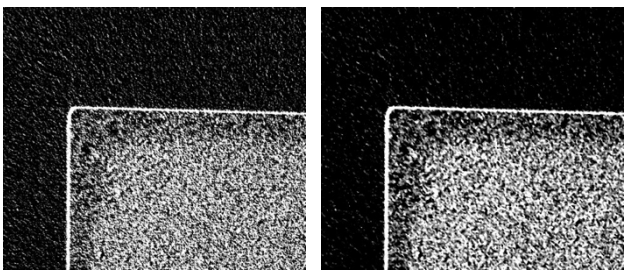

Figure 66: Application of the filter does not completely eliminate the presence of noise.

4.2 Porosity change

Figure 67 shows the evolution of the carbonation in OPS paste at 7, 14, and 22 days of carbonation monitored by using the dual CT scan method. From each sample, a slice of 13.3 x 7 x 0.7 mm was obtained and analyzed. The porosity profiles along section A-A' are shown in Figure 68; each plot is the average porosity of 100 voxels, i.e. 0.7 mm of the slice thickness.

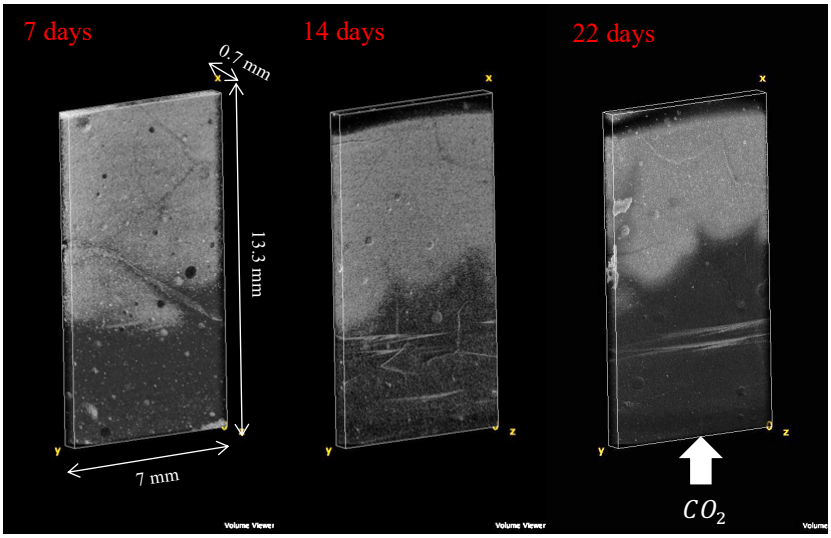

Figure 67: OPS 3D distribution of the porosity at 7, 14 and 22 days of carbonation.

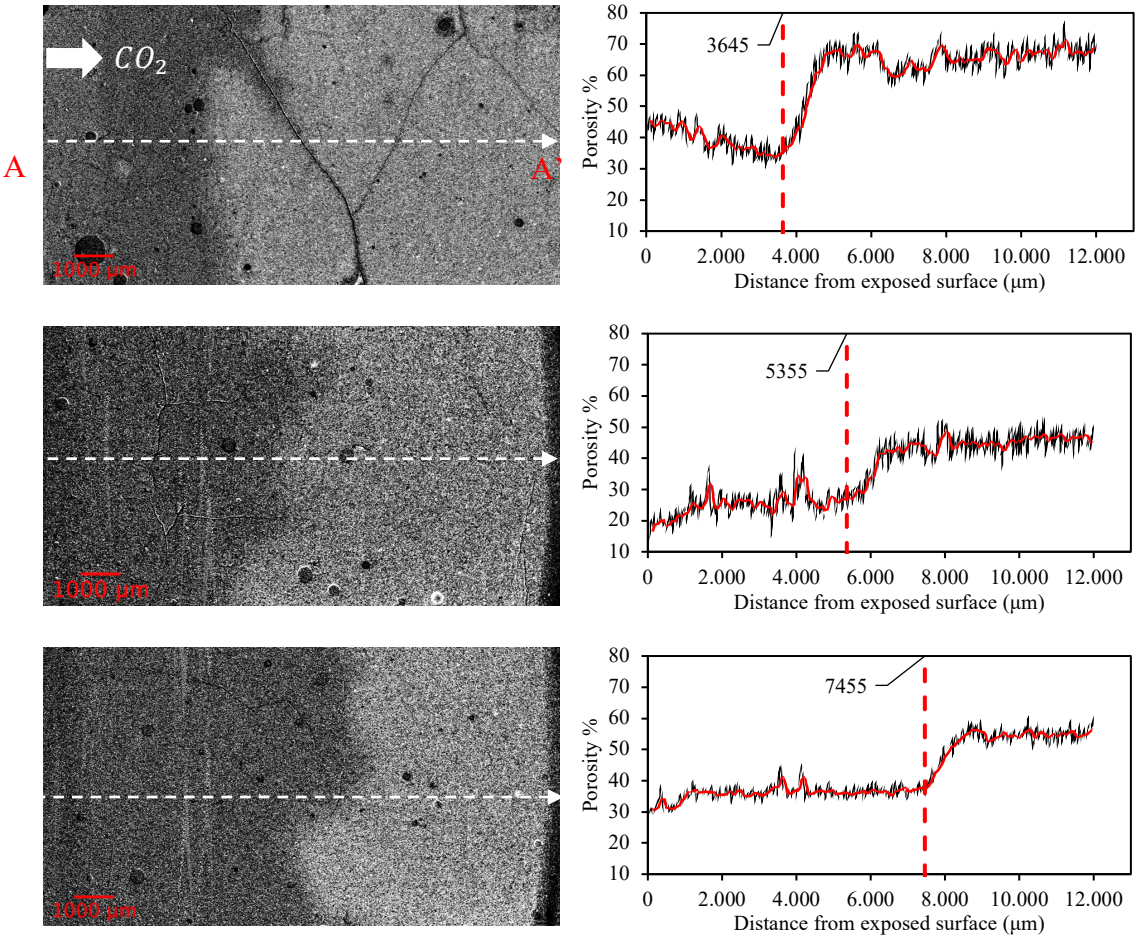

Figure 68: Typical CT images extracted from OPS samples carbonated at 7, 14, 22 days and porosity profiles along section A-A' (on the right).

Figure 69 shows the evolution of the carbonation in SLAG cement paste at 7, 14, and 22 days of carbonation monitored by using the dual CT scan method. From each sample, a slice of 13.3 x 7 x 0.7 mm was obtained and analyzed. The porosity profiles along section A-A' are shown in Figure 70.

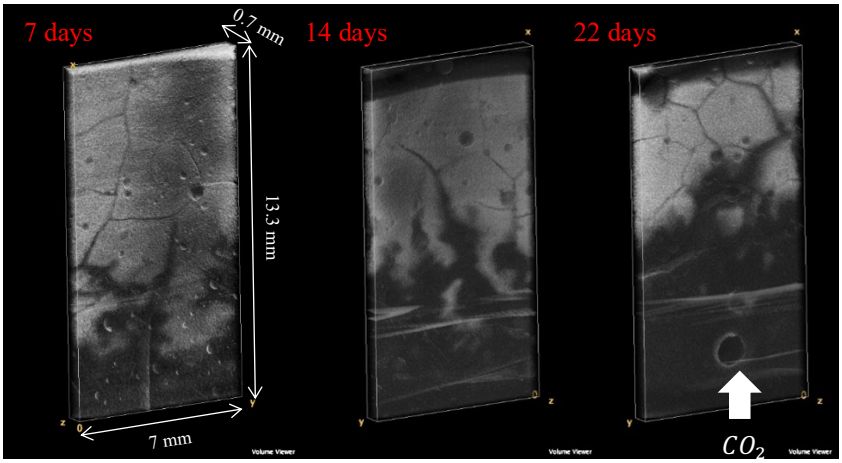

Figure 69: SLAG 3D distribution of the porosity at 7, 14 and 22 days of carbonation.

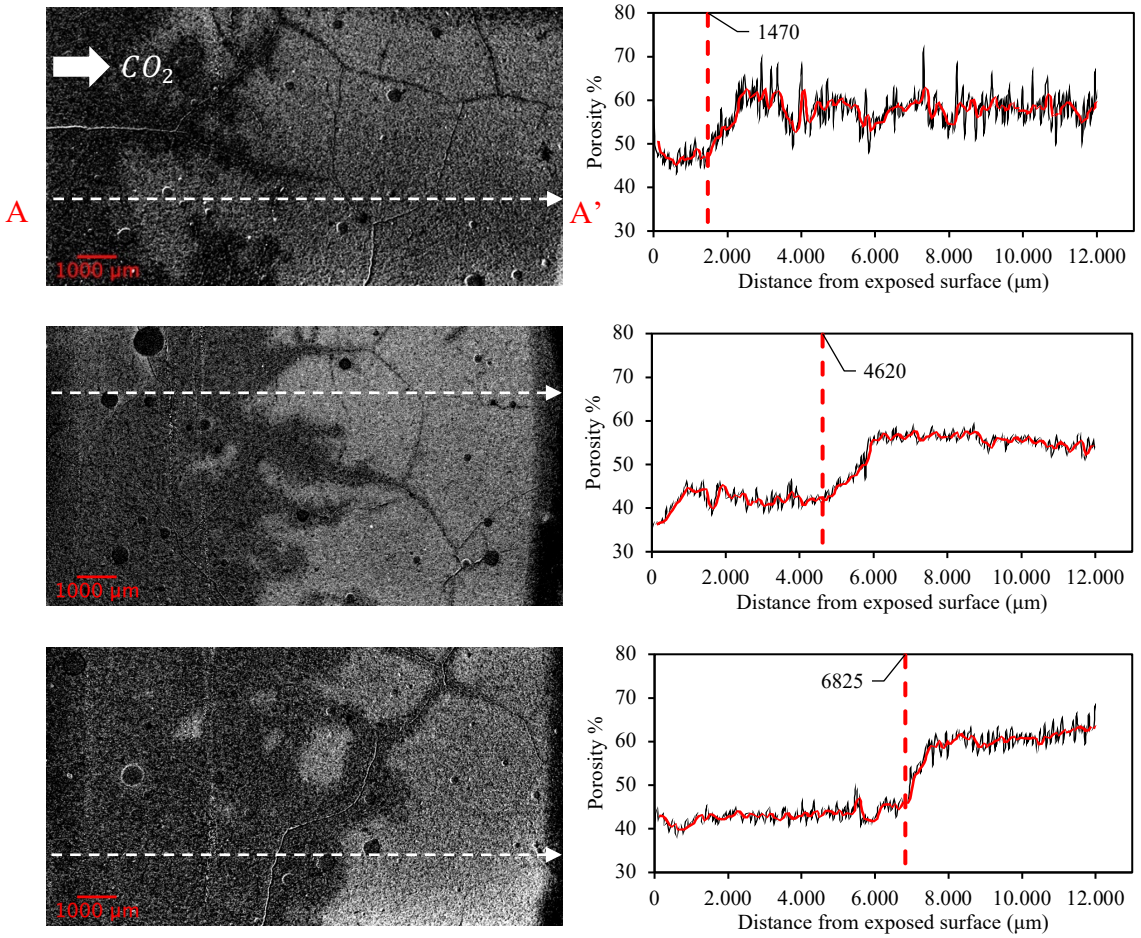

Figure 70: Typical CT images extracted from SLAG samples carbonated at 7, 14, 22 days and porosity profiles along section A-A' (on the right).

From the results, the carbonated part of the sample can be easily recognized: the uncarbonated part looks brighter while the carbonated one is darker, and brighter the area, higher is its porosity. It is also very evident that the carbonated area is getting larger over time. If we look at the shape of the carbonation front, it was possible to notice that in OPS the progress of the carbonation front is quite perpendicular to the CO_2 penetration direction, while in the SLAG cement the front is "branched", and it seems to follow the paths of the crack. This phenomenon was not observed by the phenolphthalein test. It was observed by plotting the local porosity profile that the change in porosity occurred in a "transition" zone where the GSV changes progressively. This "transition" zone is about 1 mm wide both in OPS and SLAG cement.

By comparing the different methods used to assess the carbonation depth (Figure 71), good consistency in OPS was found between phenolphthalein test and the dual scan method as shown in Figure 72, although in SLAG cement the phenolphthalein depth is higher. The carbonation depth assessed by means of the calcium carbonate profile is always higher both in OPS and in SLAG cement.

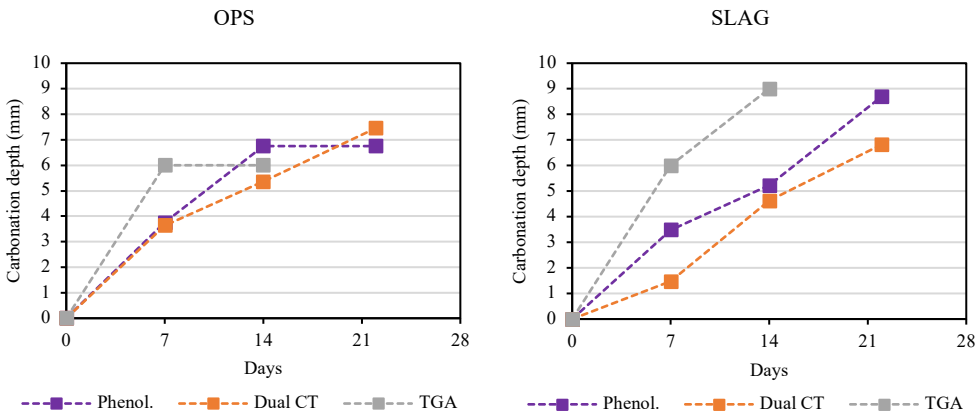

Figure 71: Comparison of different methods used to monitor the carbonation depth over time.

The phenolphthalein spray test is a simple method to assess the extent of carbonation depth by spraying a solution of phenolphthalein in diluted alcohol on the freshly broken surface of the cement paste. After treating the surface with the solution, the non-carbonated part will be pink, whereas the carbonated part will remain uncolored. The phenolphthalein test measures the pH (it will become pink above about 9.5).

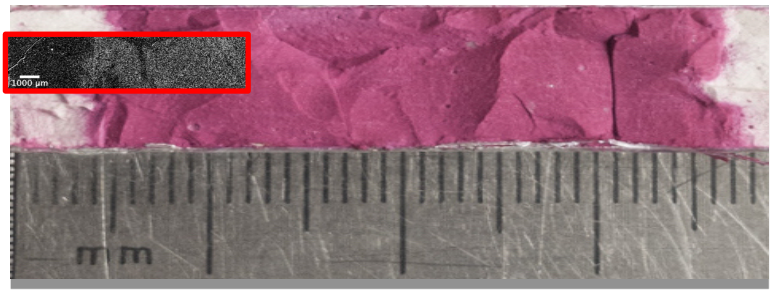

Figure 72: Comparison between carbonation depth assessed my means of phenolphthalein test and dual scan method on partially carbonated OPS sample.

A comparison of the different methods used to measure porosity is shown in Figure 73. The total porosity of uncarbonated and carbonated part was obtained from each porosity profile and compared to other methods, namely dual scan method performed on micro-beams, hydrostatical weighing, and dynamic vapor sorption. An overall decrease in porosity was observed both in ordinary Portland cement pastes and blended cement paste following carbonation.

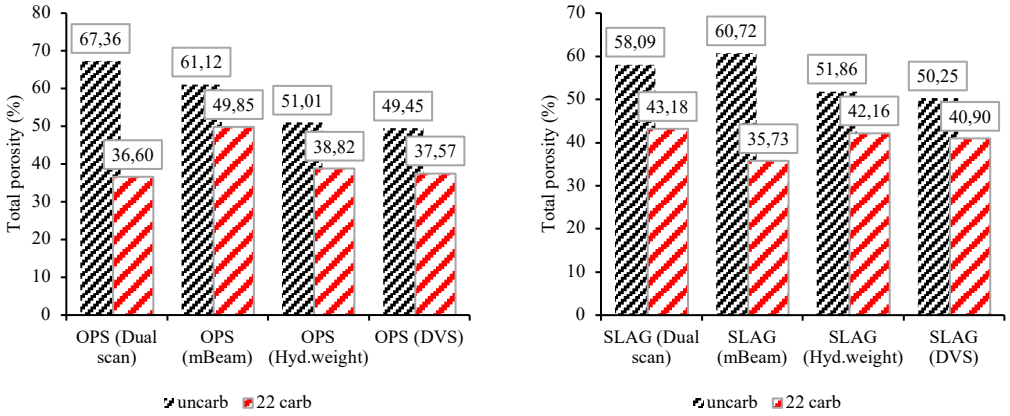

Figure 73: Comparison of the different methods used to measure the porosity and its variation following carbonation.

The fractional volume of CSH gel pores ($d \leq 0.01\mu m$) and capillary pores before and after carbonation is shown in Figure 74. An overall reduction of CSH gel porosity fraction was observed in all the material tested, whereas the capillary porosity fraction remained unchanged. Moreover, although all the materials have almost the same bulk porosity, the pore size distribution varies: SLAG cement paste, compare to ordinary Portland cement has a higher fractional volume of CSH gel pores; consequently, its pore structure is finer. However, it was found that after carbonation, its capillary porosity fraction slightly increased.

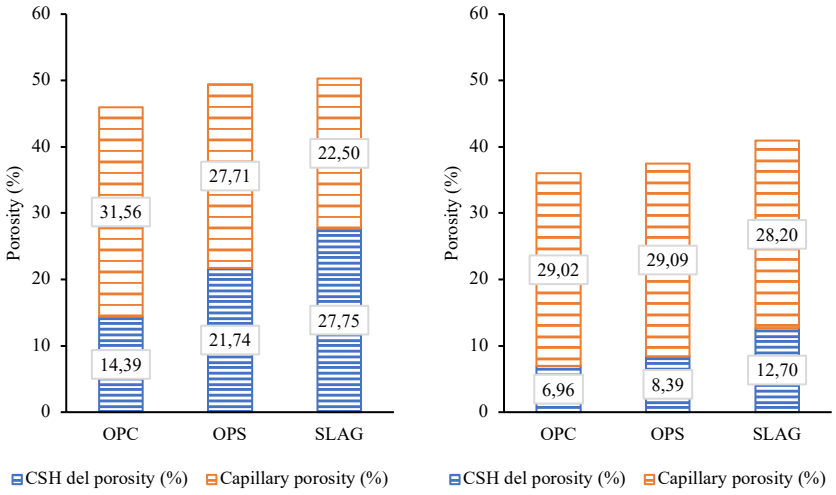

Figure 74: Fractional volume of CSH gel pores and capillary pores, based on BHJ methods, assessed before and after carbonation

4.3 Chemical composition change

The degree of hydration calculated through the equation proposed by Bhatty are listed in Table 7.

$$Degree\ of\ hydration = \frac{(Ldh + Ldx) + 0.41(Ldc)}{0.24}$$

	Degree of hydration (at 90 days)
OPC	85%
OPS	91%
SLAG	85%

Table 7: Degree of hydration after 90 days.

The Portlandite and carbonates profile of OPC, OPS, and SLAG are represented in Figure 75 and 76 respectively. By analyzing the OPC profiles at 0, 14, and 22 days of carbonation, it was possible to notice that:

- After 14 days of exposure, the portlandite content (CH%) dropped significantly but not completely depleted. The maximum carbonation degree of portlandite is 0.5, assessed after 14 days: the amount of portlandite decreased from 22.15%wt to about 11%wt, and the value remained the same after 22 days of carbonation as well
- The rate of portlandite carbonation was very fast in the early days and then slowed down. This behavior is related to the formation of calcium carbonate layer around the portlandite crystals, which prevent further carbonation of portlandite [39].

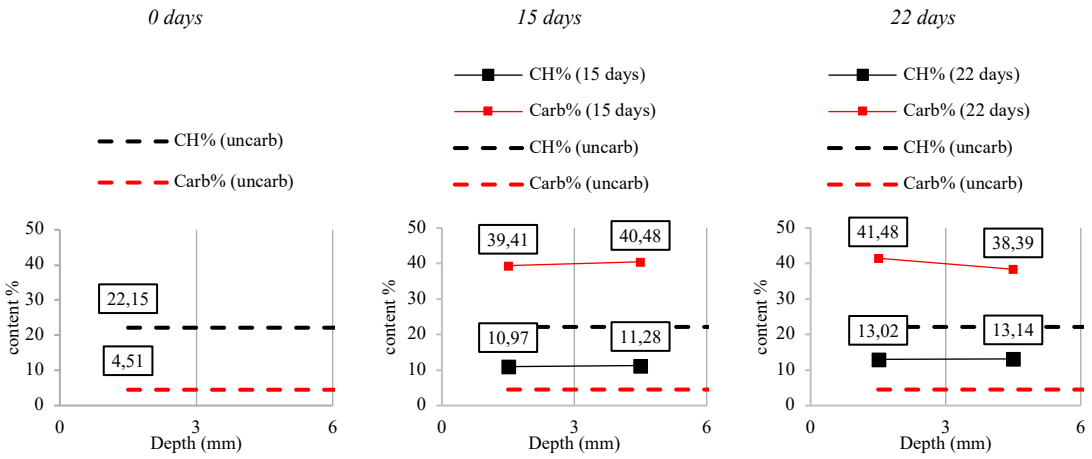

Figure 75: Portlandite and calcium carbonates profiles of OPC at 0, 14, and 22 days of carbonation.

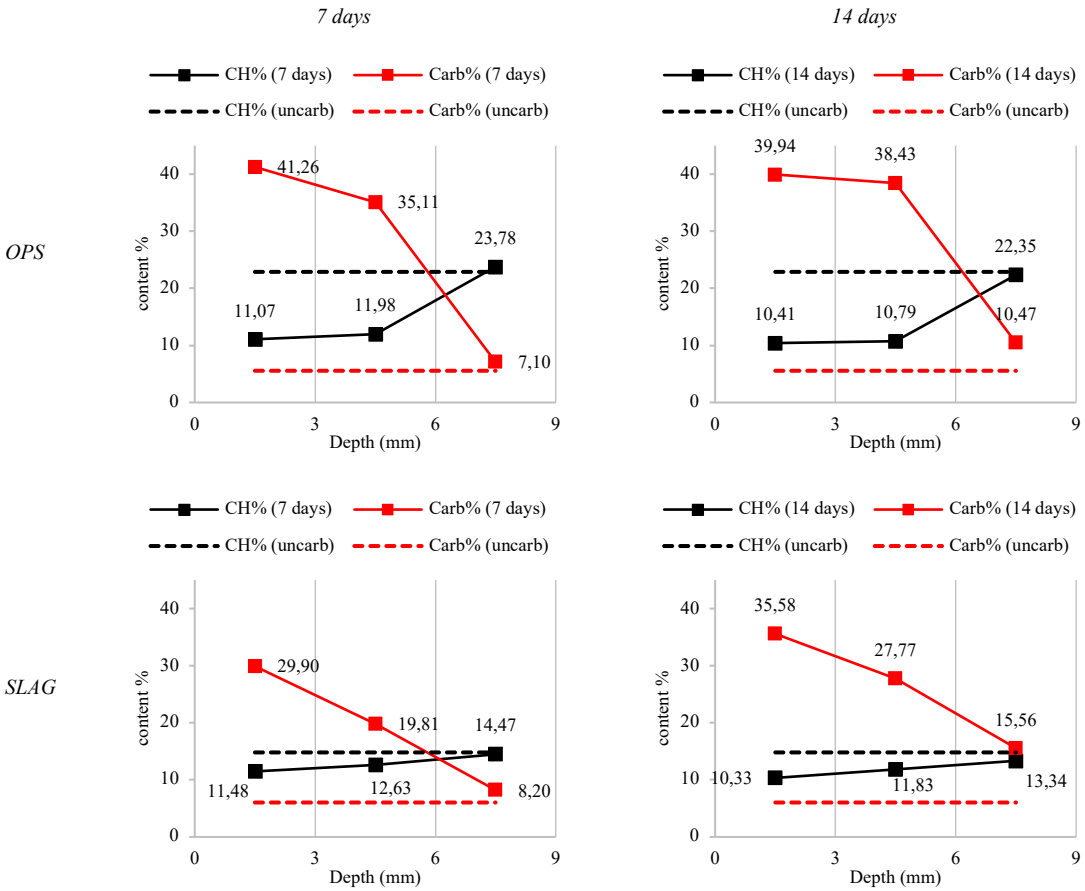

Figure 76: Portlandite and calcium carbonates profiles of OPS and SLAG cement pastes at 0, 7, and 14 days of carbonation.

OPS behaves the same way of OPC: same initial portlandite and calcium carbonate content respectively 22.88% and 5.56%, as well as after 14 days of carbonation (10.41% CH and 39.94% calcium carbonate). However, it must be noted that after 7 days of carbonation, the calcium carbonate content in the first 3mm of depth was already stable. Therefore, after 7 days, portlandite seems to no longer react with carbon dioxide. As expected, the blended cement paste (OPC/40% BFS) has a lower initial portlandite content (14.80%wt), due to its consumption in the pozzolanic reaction. The general trend of the profiles remained the same: increase of the calcium carbonate content and decrease of the portlandite, but it is possible to notice that:

- After 14 days the precipitation of calcium carbonate particles in the pore space is no longer the main reason for the change in porosity in OPS, this is also in agreement with the porosity quantification between 14 and 22 days (Figure 77).
- The portlandite dissolution rate between 7 and 14 days in SLAG was much lower with respect to the increased rate of calcium carbonate content, as shown in Figure 76: this can be explained by the fact that the carbonation of portlandite is not predominant respect to the carbonation of other phases such as CSH.
- The carbonation mechanism of blended cement paste is slower respect to OPC and continues to proceed after 7 days. It can be noticed in the Figure 76 that the portlandite content in SLAG is still dropping after 7 days while the calcium carbonate was increasing. This is also in accordance with the porosity change shown in Figure 78.

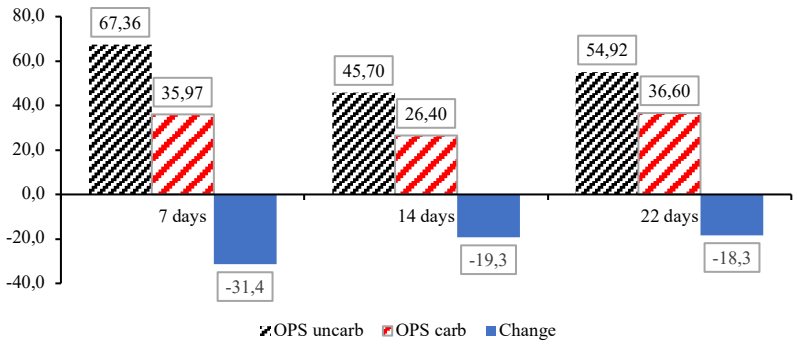

Figure 78: OPS porosity evolution at 7, 14, and 22 days of carbonation monitored by using dual CT scan method.

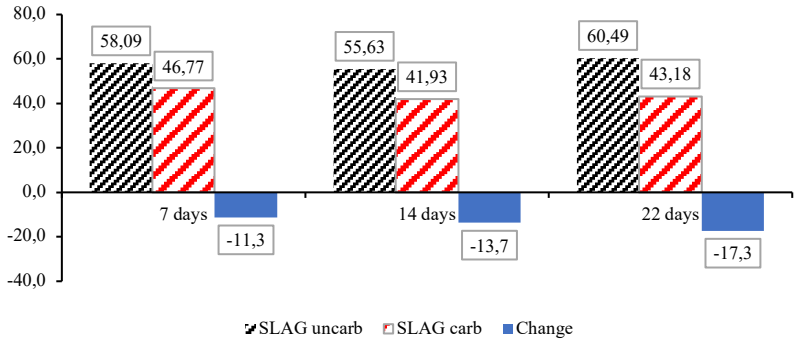

Figure 77: SLAG porosity evolution at 7, 14, and 22 days of carbonation monitored by using dual CT scan method.

4.4 Water vapor sorption isotherms

By analyzing the water desorption isotherm of OPC, OPS and SLAG cement pastes before and after 22 days of carbonation, a drop of the water content over all the relative humidity range was observed, which can be explained as a consequence of porosity reduction (Figure 79). Although in blended cement paste it was more pronounced in the range above 30%RH.

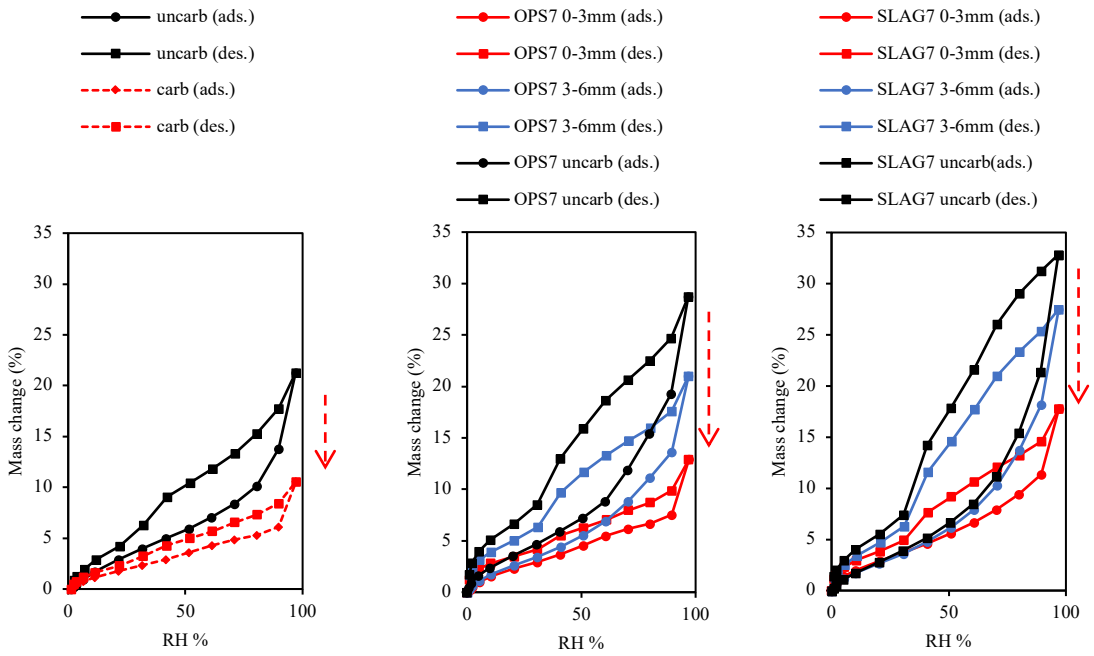

Figure 79: Effect of carbonation on water vapor sorption isotherms of OPC, OPS, and SLAG.

Figure 80, shows the change of the water retention curve following carbonation, and it was found an increase in the water retention capacity in the range from 0%RH to 40%RH, and on the contrary a decrease in the range from 40%RH to 100%RH, in all the material tested, although this phenomenon is more pronounced in the material subjected to moist curing (OPS and SLAG). The alteration of the water retention curve shape can be related to the pore size distribution alteration.

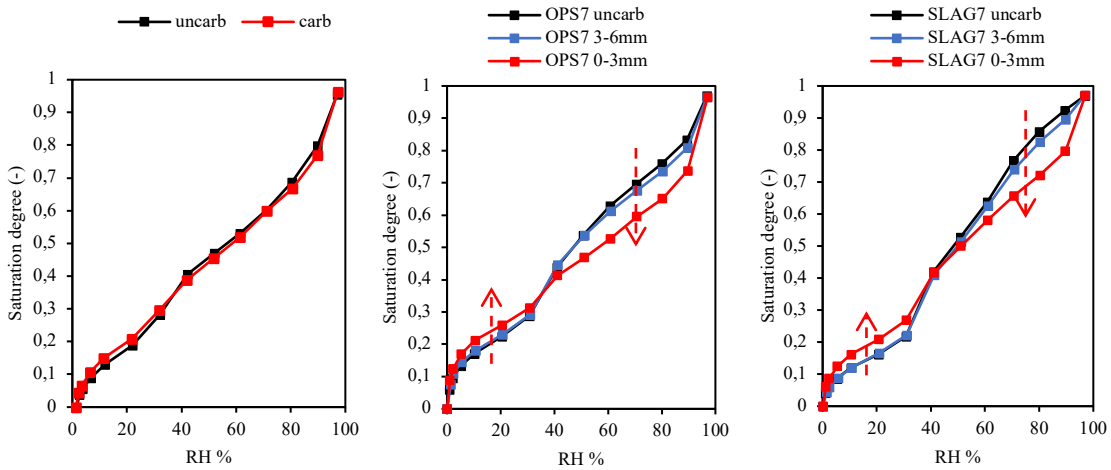

Figure 80: Effect of the carbonation on water retention curves of OPC, OPS, and SLAG.

The parameters used to calculate the relative permeability coefficient and obtained by fitting the Van Genuchten analytical formula (equation 23) to experimental capillary pressure are listed in Table 8.

Material	OPC uncarb	OPC22 3-6mm	OPS7 uncarb	OPS7 3-6mm	OPS7 0-3mm	SLAG7 uncarb	SLAG7 3-6mm	SLAG7 0-3mm
a (Mpa)	70,8734	72,4619	72,5790	63,1229	56,6714	62,3371	63,7854	61,9649
b (-)	1,6257	1,6539	1,7963	1,8999	2,0218	1,7409	1,7204	1,8394

Table 8: Best fitting parameters for Van Genuchten model.

Figure 81 shows the effect of carbonation on the saturation dependent permeability coefficient.

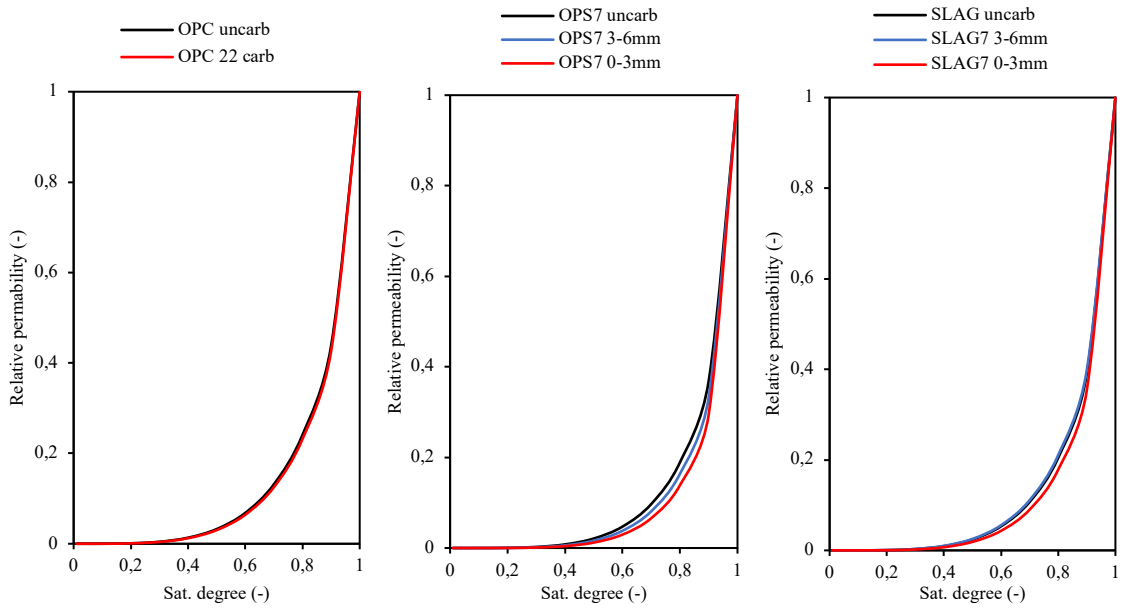

Figure 81: Relative permeability coefficient vs. saturation degree assessed using the Mualem's model.

A reduction of the relative permeability coefficient was found in OPS which is directly related to the reduction of the parameter "a" obtained from the V. Genuchten model as shown in Table 8, whereas there were no significant changes in OPC and SLAG.

4.5 Tortuosity

Limiting slopes of the mean square-displacement $r^2(t)$ are reposted in Figure 82. Tortuosity is calculated as the inverse of the limiting slope of $r^2(t)$. It was observed that carbonation led to increasing the tortuosity in all the tested materials, as shown in Figure 83.

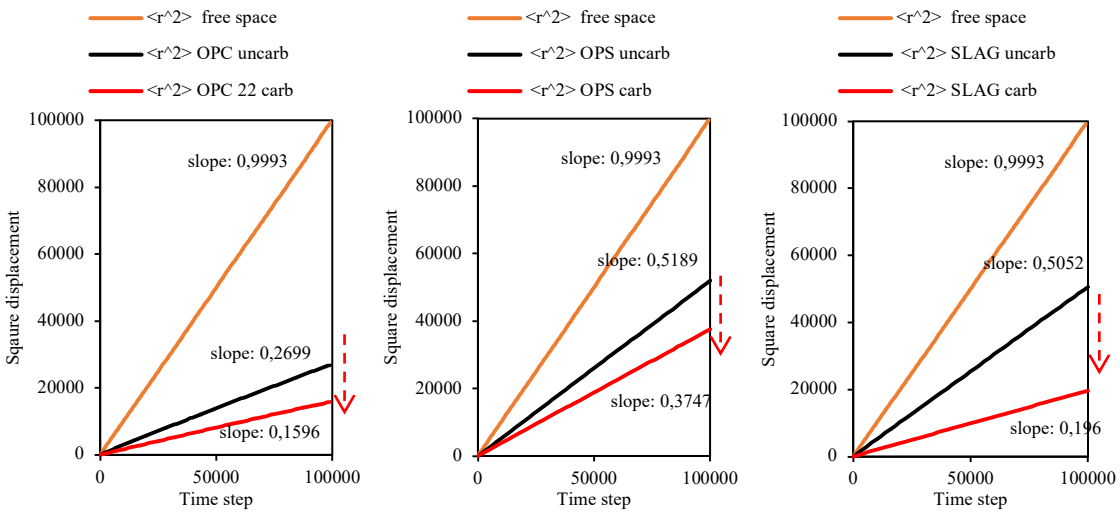

Figure 82: Limiting slope of the mean square-displacement before (dark) and after carbonation (red).

$$\tau_g = \left[\lim_{t\to\infty} \frac{dr^2(t)}{dt}\right]^{-1}$$

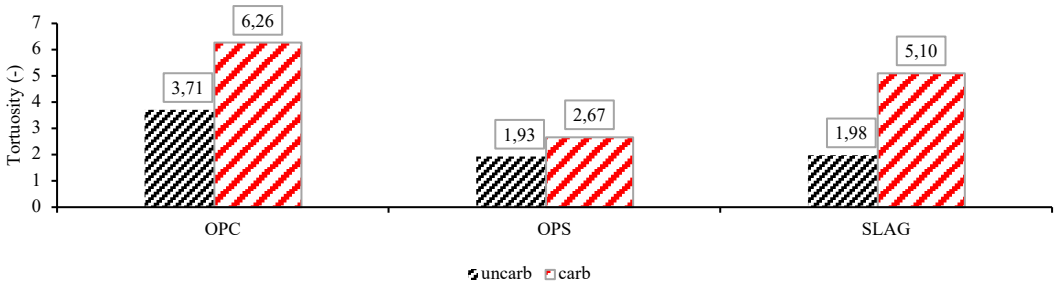

Figure 83: Effect of the carbonation on tortuosity.

4.6 Intrinsic permeability

Using both physical model (Katz-Thompson) and LB simulation, a decrease of the intrinsic permeability was observed after carbonation of OPC, although simulated permeability coefficient by using PALABOS is lower compared to those assessed by means of the Katz-Thompson model, four times lower in the non-carbonated state (Figure 84), while good consistency was found in the carbonated state.

$$K_I = \frac{1}{226}\frac{\sigma}{\sigma_0} l_c^2$$

where $\frac{\sigma}{\sigma_0}$ was obtained from the Nernst-Einstein relation (in which tortuosity is required) and critical length l_c was obtained from MIP test.

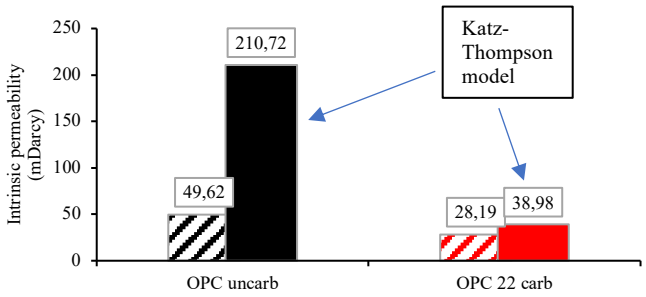

Figure 84: Comparison between physical model based and simulation based instinct permeability of OPC.

All the results of LB simulations are showed in Figure 85. Good consistency was found between OPC and OPS.

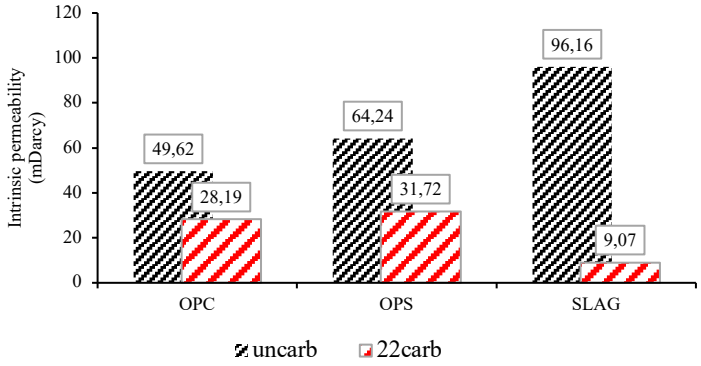

Figure 85: Effect of carbonation on intrinsic permeability.

5 Discussion

Both tortuosity and CSH gel porosity were correlated with the intrinsic permeability coefficient. The influence of tortuosity on permeability can be described by a logarithmic law (Figure 87), and the results are in line with the expectation: high tortuosity corresponds to low permeability coefficient. However, the amount of CSH gel porosity seems to be a good parameter to predict permeability; in fact, a linear function fits quite good to experimental data, as shown in Figure 86.

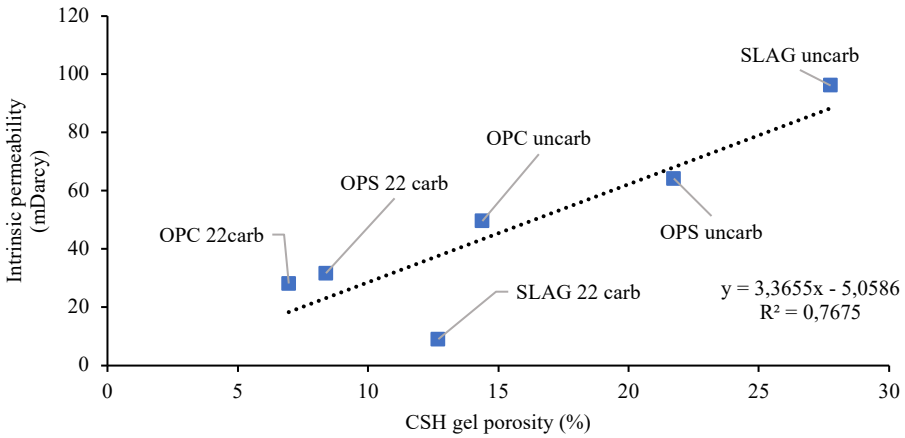

Figure 86: Influence of CSH gel porosity fraction on the intrinsic permeability.

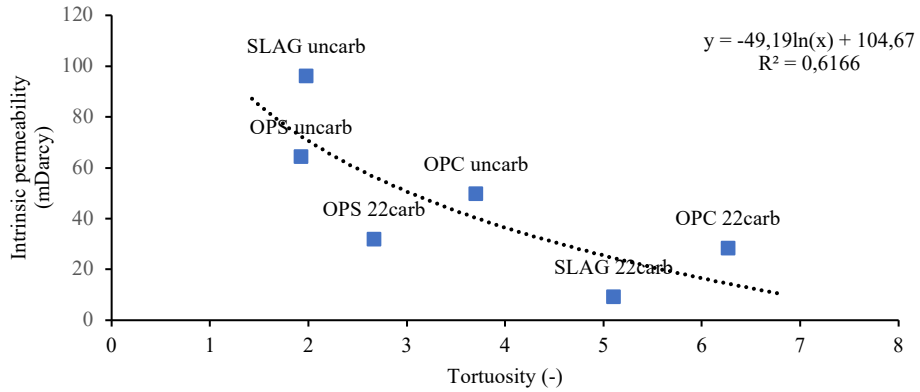

Figure 87: Influence of tortuosity on the intrinsic permeability.

A good logarithmic correlation was found between tortuosity and total porosity assessed on micro-beams by using the dual scan method (Figure 88).

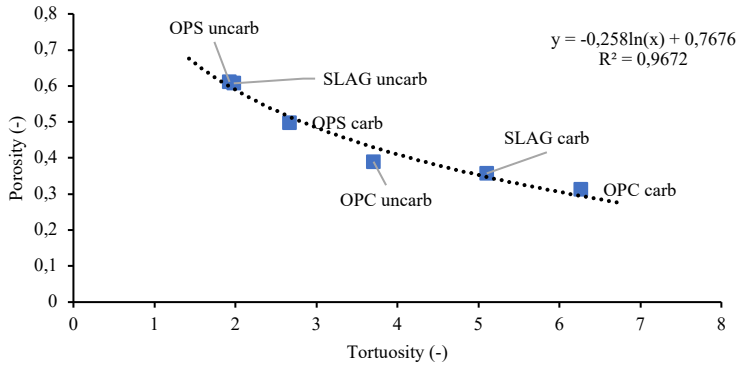

Figure 88: Correlation between porosity assessed on micro-beam and simulated tortuosity.

A reduction of the relative permeability coefficient following carbonation was found in all the materials tested as shown in the Figure 89, in which the variation of the relative permeability coefficient in term of absolute variance is plotted against saturation degree. Variations occurred almost over the whole saturation degrees, although maximum variations are located in high saturation degree range, and more precisely at 0.95. By comparing the two types of cement pastes, ordinary Portland cement pastes had higher variations, almost twice, compared to blended cement paste.

Since in this study the relative permeability coefficient has been assessed by using the Mualem's model which is in turn related to the Van Genuchten's model, it must be noted that OPC fitting parameters of the Van Genuchten's model are not reliable in high saturation degree range [35], as shown in Figure 87.

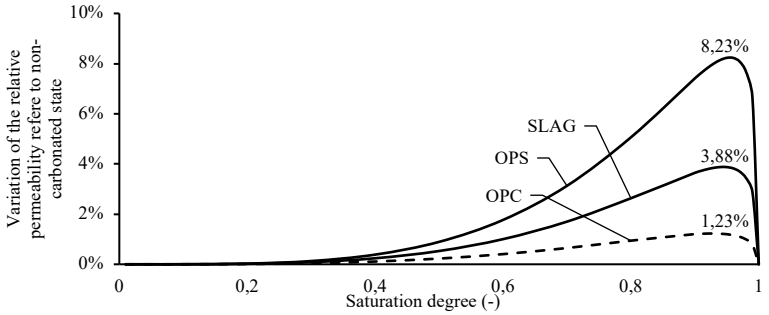

Figure 89: Effect of the carbonation on the relative permeability coefficient in term of absolute variance between non-carbonated and carbonated relative permeability coefficient.

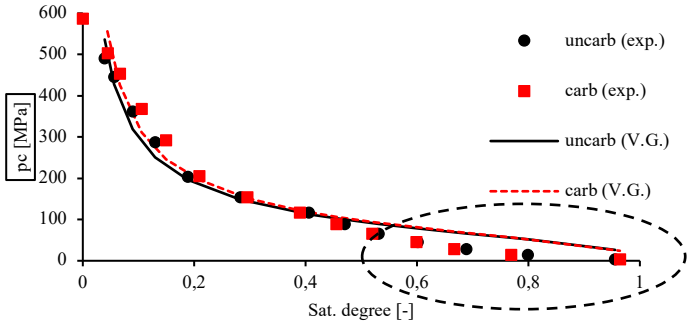

Figure 90: Weakly reliability of the V. Genuchten model in high saturation range.

6 Conclusion

The effect of carbonation was studied using two types of material, namely Ordinary Portland cement paste and Blended cement paste (OPC/40% BFS). The impact of carbonation was evaluated on pore size distribution, porosity, hydrated phases composition, water sorption isotherms, tortuosity, and permeability. All the pastes were cured up to 90 days, followed by 14 days of conditioning at 65%RH and then carbonated in accelerated conditions (5%CO_2, 65%RH and 20°C). As an alternative to traditional tests to evaluate the porosity of cement pastes, the X-ray microtomography was used to monitor the change in porosity due to carbonation, and to overcome some limitation of traditional CT scan such as limited spatial resolution and pore segmentation technique, the dual CT scan method was performed. The methodology was validated by using MIP and hydrostatical weighing methods, and it was found that the dual CT scan methodology has detected the change in porosity which occurred in the pore size range below 0.1µm which is over one order of magnitude higher than the maximum spatial resolution obtained with a single CT scan (7.0µm). Despite this, the porosity measured is overestimated.

A drop of porosity after carbonation was found in all the material tested, which mainly occurred in the range size below 0.01µm. By analyzing the TGA results, carbonation of ordinary Portland cement occurred mainly in the early days during which the calcium carbonate content rapidly increases up to 40%wt while on the contrary portlandite dissolved but not completely depleted. The maximum carbonation degree of portlandite, which is the main hydrated phase, was 0.5 reached after 7 days. In blended cement paste the carbonation kinetics is slower compared to OPC and by comparing the dissolution rate of portlandite to the precipitation rate of calcium carbonite, led to the conclusion that carbonation of CSH was predominant in blended cement paste, although it has not produced an increase in porosity as expected from the literature.

Dynamic Vapor Sorption machine was adopted to carry out the water vapor sorption isotherm experiments, and from which it was possible to obtain the following information:

- The reduction of the porosity was confirmed by the test. A drop of the water content over all the relative humidity range was observed both in OPC and SLAG.
- Change in porosity mainly occurred in the pore range below 0.01µm, according to BHJ method.
- A similar variation of the water retention curve was found in all the material tested after carbonation, namely an increase of the retention capacity between 0%RH and 40%RH, and a reduction in capacity between 40%RH and 100%RH.
- In blended cement paste, unlike OPC, an increase of the capillary porosity was found after carbonation while the CSH gel amount has not changed, unexpectedly.
- Moreover, as a general trend, an increase of the capillary pressure was found after carbonation.
- From the experimental data, the unsaturated relative permeability coefficient can be obtained by using Mualem's model.

Tortuosity and intrinsic permeability coefficient were obtained by simulation using as input CT images coming from the microbeams scan. The maximum resolution reached was 0.63µm, which is close to synchrotron CT. The dual scan method was used as an alternative to the traditional pore segmentation process, then from each sample cubic volumes of 256 x 256 x 256 voxels (i.e. 161.3 x 161.3 x 161.3 μm^3) were extracted. A good correlation between tortuosity and intrinsic permeability coefficient was found, whereas the permeability coefficient is highly correlated with the CSH gel porosity measured by means of

the water vapor sorption isotherm experiments. It was found that carbonation led to increasing the tortuosity and, in line with the expectation, to decrease the permeability.

7 References

[1]. P. Kumar Mehta, Paulo J. M. Monteiro, Concrete: Microstructure, Properties, and Materials, 2006.

[2]. Karen, L. S., Impact of microstructure on the durability of concrete. Second International Conference on Microstructural-related Durability of Cementitious Composites, 11-13 April 2012, Amsterdam, The Netherlands.

[3]. Guang Ye, Experimental Study and Numerical Simulation of the Development of the Microstructure and Permeability of Cementitious Materials, 2003.

[4]. Véronique Baroghel-Bouny, Water vapour sorption experiments on hardened cementitious materials, Part I: Essential tool for analysis of hygral behaviour and its relation to pore structure, 2006.

[5]. Véronique Baroghel-Bouny, Water vapour sorption experiments on hardened cementitious materials, Part II: Essential tool for assessment of transport properties and for durability prediction, 2006.

[6]. Olivier Coussy, Poromechanics, 2004.

[7]. M.A. Peter, A. Muntean, S.A. Meier, M. Böhm, Competition of several carbonation reactions in concrete: A parametric study, 2008.

[8]. Branko Šavija, Mladena Luković, Carbonation of cement paste: Understanding, challenges, and opportunities, 2016.

[9]. Nelie De Belie et al., A Review of Self-Healing Concrete for Damage Management of Structures, 2018.

[10]. B. Wu, G, Ye, Development of porosity of cement paste blended with supplementary cementitious materials after carbonation, 2017.

[11]. V.T. Ngala, C.L. Page, EFFECTS OF CARBONATION ON PORE STRUCTURE AND DIFFUSIONAL PROPERTIES OF HYDRATED CEMENT PASTES, 1997.

[12]. Martin Auroy , Stéphane Poyet, Patrick Le Bescop, Jean-Michel Torrenti, Thibault Charpentier, Mélanie Moskura, Xavier Bourbon, Impact of carbonation on unsaturated water transport properties of cement-based materials, 2015.

[13]. Quoc Tri Phung, Norbert Maes, Diederik Jacques, Els Bruneel, Isabel Van Driessche, Guang Ye, Geert De Schutter, Effect of limestone fillers on microstructure and permeability due to carbonation of cement pastes under controlled CO2 pressure conditions, 2015.

[14]. A.M. Neville, Properties of Concrete, 2011.

[15]. H. Cui et al., Experimental study on effects of CO2 concentrations on concrete carbonation and diffusion mechanisms, 2015.

[16]. M. Thiéry, Paméla Faure, Antoine Morandeau, Gérard Platret, Jean-François Bouteloup, Patrick Dangla, Véronique Baroghel-Bouny, Effect of Carbonation on the Microstructure and Moisture Properties of Cement - Based Materials, 2011.

[17]. Z. Osmanovic, Nedzad Haračić, Jelica Zelic, Properties of blastfurnace cements (CEM III/A, B, C) based on Portland cement clinker, blastfurnace slag and cement kiln dusts, 2018.

[18]. J.F. Young, HUMIDITY CONTROL IN THE LABORATORY USING SALT SOLUTIONS – A REVIEW, 1967.

[19]. Hongyan Ma, Mercury intrusion porosimetry in concrete technology: Tips in measurements, pore structure parameter acquisition and application, 2014.

[20]. C. Hall and W.D. Hoff, Water Transport in Brick, Stone and Concrete, 2012.

[21]. Jie Zhang, George W. Scherer, Comparison of methods for arresting hydration of cement, 2011.

[22]. Karen Scrivener, Ruben Snellings, Barbara Lothenbach, A Practical Guide to Microstructural Analysis of Cementitious Materials, 2016.

[23]. J.I. Bhatty, Reid, K.J., Dollimore, D., Gamlen, G. A., Mangabhai, R. J. Rogers, P.F., and Shah, T.H., The Derivation of Kinetic Parameters in Analysis of Portland Cement for Portlandite and Carbonate by Thermogravimetry, 1988.

[24]. R.A. Olson, H.M. Jennings, Estimation of C-S-H content in a blended cement paste using water adsorption, 2000.

[25]. Jiande Han, Ph.D; Wei Sun; Ganghua Pan; Wang Caihui, Ph.D., Monitoring the Evolution of Accelerated Carbonation of Hardened Cement Pastes by X-Ray Computed Tomography, 2013.

[26]. S. Lu, E. N. Landis, D. T. Keane, X-ray microtomographic studies of pore structure and permeability in Portland cement concrete, 2006.

[27]. M.A.B. Promentilla, T. Sugiyama, T. Hitomi, N. Takeda, Quantification of tortuosity in hardened cement pastes using synchrotron-based X-ray computed microtomography, 2009.

[28]. Degruyter W., Bachmann O., Burgisser A., Malaspinas O. A synchrotron perspective on gas flow through pumices, 2010.

[29]. Dong Cui, Nemkumar Banthia, Qiannan Wang, Wei Sun, Investigation on porosity of partly carbonated paste specimens blended with fly ash through dual CT scans, 2019.

[30]. Keshu Wan, Qiong Xu, Lin Li, Wei Sun, 3D porosity distribution of partly calcium leached cement paste, 2013.

[31]. Dong Cui a, Wei Sun, Qiannan Wang, Chunping Gu, Use of tomography to estimate the representative elementary volume in mortars stained with potassium iodide, 2018.

[32]. Kenshu Wan, Xu Qiong, Local porosity distribution of cement paste characterized by X-ray micro-tomography, 2013.

[33]. Yoshito NAKASHIMA, Susumu KAMIYA, Mathematica Programs for the Analysis of Three- Dimensional Pore Connectivity and Anisotropic Tortuosity of Porous Rocks using X-ray Computed Tomography Image Data, 2012.

[34]. Yidong Gan, Branko Šavija, Hongzhi Zhang, Erik Schlangen, Static and Fatigue Tests on Cementitious Cantilever Beams Using Nanoindenter, 2018.

[35]. Marc Mainguy, Isothermal drying process in weakly permeable cementitious materials – Assessment of water permeability, 1999.

[36]. Alessandro Ciani, M.Sc thesis: Lattice Boltzmann Methods for Single and Two-Phase Flows in Porous Media: Theory and Applications, Politecnico di Milano, 2012-2013.

[37]. Mingzhong Zhang, Multiscale Lattice Boltzmann-Finite Element Modelling of Transport Properties in Cement-based Materials, 2013.

[38]. W. J. Weiss, T. J. Barrett, C. Qiao, H. Todak, Toward a Specification for Transport Properties of Concrete Based on the Formation Factor of a Sealed Specimen, 2016.

[39]. Vineet Shaha, Karen Scrivenerb, Bishwajit Bhattacharjeea, Shashank Bishnoi, Changes in microstructure characteristics of cement paste on carbonation, 2018.

[40]. M.A. Sanjuan, C. Andrade, M. Cheyrezy, Concrete carbonation tests in natural and accelerated conditions, 2003.

[41]. Martin Auroya, Stéphane Poyeta, Patrick Le Bescopa, Jean-Michel Torrentib, Thibault Charpentierc, Mélanie Moskurac, Xavier Bourbond, Comparison between natural and accelerated carbonation (3% CO2): Impact on mineralogy, microstructure, water retention and cracking, 2018.

[42]. Marta Castellote, Lorenzo Fernandez, Carmen Andrade, Cruz Alonso, Chemical changes and phase analysis of OPC pastes carbonated at different CO2 concentrations, 2009.

[43]. H.M. Jennings, Colloid model of CSH and implications to the problem of creep and shrinkage, 2004.

[44]. ACI Committee 201, ACI 201.2R-16, Guide to Durable Concrete, 2016,

[45]. https://www.ugent.be/ea/structural-engineering/en/research/magnel/research/research3/selfhealing
[46]. https://www.egr.msu.edu/~kutay/LBsite/index.htm
[47]. http://www.palabos.org/documentation/tutorial/permeability.html
[48]. https://staff.aist.go.jp/nakashima.yoshito/index-e.htm
[49]. Nakashima, Y. and Nakano, T. (2012) Steady-State Local Diffusive Fluxes in Porous Geo-Materials Obtained by Pore-Scale Simulations. Transport in Porous Media 93, 657-673.
[50]. Shackelford, C. D, 1991, Laboratory diffusion testing for waste disposal—a review, Journal of Contaminant Hydrology, 7(3), pp. 177-217.
[51]. Mario Collepardi, Silvia Collepardi, Roberto Troli, IL NUOVO CALCESTRUZZO (sesta edizione), 2014, pag. 153-154.